

An initial study of interference coloration for quantifying the texture and fabric of ice

Owen, Cody C.; Hendrikse, Hayo

DOI

[10.1016/j.coldregions.2022.103735](https://doi.org/10.1016/j.coldregions.2022.103735)

Publication date

2023

Document Version

Final published version

Published in

Cold Regions Science and Technology

Citation (APA)

Owen, C. C., & Hendrikse, H. (2023). An initial study of interference coloration for quantifying the texture and fabric of ice. *Cold Regions Science and Technology*, 206, Article 103735. <https://doi.org/10.1016/j.coldregions.2022.103735>

Important note

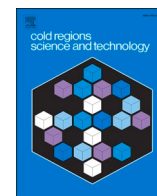
To cite this publication, please use the final published version (if applicable). Please check the document version above.

Copyright

Other than for strictly personal use, it is not permitted to download, forward or distribute the text or part of it, without the consent of the author(s) and/or copyright holder(s), unless the work is under an open content license such as Creative Commons.

Takedown policy

Please contact us and provide details if you believe this document breaches copyrights. We will remove access to the work immediately and investigate your claim.



An initial study of interference coloration for quantifying the texture and fabric of ice

Cody C. Owen^{*}, Hayo Hendrikse

Department of Hydraulic Engineering, Delft University of Technology, Delft, The Netherlands

ARTICLE INFO

Keywords:

Birefringence
Image processing
Ice microstructure
Grain boundary
c-axis

ABSTRACT

The manual application of universal (Rigsby) stage techniques is commonly used to determine the fabric of thin sections of ice viewed with crossed-polarized light. This process can require hours of focus in cold conditions to identify the c-axis of each grain in a thin section. Automated ice texture and fabric methods of several forms exist but are rarely implemented beyond the field of glaciology. The present study introduces a method based on the theory of interference coloration for automated ice texture and quarter fabric analysis by using in-plane conventional photography of an ice thin section as input. The method is compatible with universal stages and polariscopes, and is not restricted by the planar-face dimensions of the thin section, allowing for thin section analysis of any size when sufficient digital camera resolution is available. Light source color temperature and chromatic adaptation are considered in the interference coloration theory, and ice fabrics are simulated for reference in identifying ice types. Sample thin section texture and quarter fabric analyses from freshwater lake and laboratory-grown ice are presented to demonstrate the applications of the method. The method is compared with the Rigsby stage technique, which yielded mean (standard deviation of) azimuth and inclination errors of 2.9 (1.0) and 11.5 (8.0) degrees, respectively, thereby demonstrating accuracy sufficient for quantifying quarter fabrics when considering a mean standard deviation in inclination of 5.4 degrees with the Rigsby stage technique.

1. Introduction

The measurement of ice microstructure—herein referring to texture and fabric (Sammonds et al., 2017; Thorsteinsson et al., 1997)—utilizing birefringence was first implemented by Rigsby (1951) on glacial ice and the technique was later elaborated by Langway (1958). Classifications of ice microstructure were then formally catalogued by Michel and Ramseier (1971) based on thin sections that were analyzed with a universal stage and the results were presented with Schmidt equal-area projection plots (also known as Wulff stereographic net or stereonets). These stereonets (from stereographic projection of spherical coordinates onto a circular plane) and other fabric methods represent the orientation distribution of the c-axes, coincident with the optic axes, of the ice grains, from which the growth and deformation histories and mechanical properties can be ascertained. Historically, ice textures were determined from scaled photographs of ice thin sections viewed between crossed polarizers (Perey and Pounder, 1958; Thorsteinsson et al., 1997).

Detailed ice textures and fabrics are evident in experiments relevant for glaciological studies (e.g. Chauve et al. (2015); Grennerat et al. (2012); Peternell et al. (2014)), but such analyses are only applied to a limited extent in freshwater and saline ice cover research (e.g. Cole et al. (1998); Schulson and Duval (2009)). One reason for this absence of ice microstructure analysis is the arduous nature of manual identification of numerous c-axes in a universal (Rigsby) stage in a subzero working environment, which is the manner by which this information is still extracted in contemporary studies (e.g. Gharamti et al. (2021); Wei et al. (2020)). Furthermore, when ice textures are made, they are still done by manually tracing grain boundaries and counting grains in a thin section or by using the linear intercept method (e.g. Snyder et al. (2015)). Instead, typically only photographs are provided of an ice thin section viewed between crossed polarizers with a reference length scale and little mention is made of the relevance of the ice texture and fabric to the mechanical behavior (e.g. Hendrikse et al. (2022); O'Rourke et al. (2016); Seymour-Pierce et al. (2017); Sinha (2011); Sopper et al. (2017); Timco and Weeks (2010)). An exception to this trend is the use of the

^{*} Corresponding author at: Delft University of Technology, Faculty of Civil Engineering and Geosciences, Department of Hydraulic Engineering, Section of Offshore Engineering, Stevinweg 1, 2628CN Delft, The Netherlands.

E-mail address: c.c.owen@tudelft.nl (C.C. Owen).

<https://doi.org/10.1016/j.coldregions.2022.103735>

Received 23 May 2022; Received in revised form 21 October 2022; Accepted 26 November 2022

Available online 2 December 2022

0165-232X/© 2022 The Authors. Published by Elsevier B.V. This is an open access article under the CC BY license (<http://creativecommons.org/licenses/by/4.0/>).

Schmid (orientation) factor to characterize the effects of alignment of the *c*-axes on the constitutive behavior of freshwater and sea ice (Azuma, 1995; Azuma, 1994; Chauve et al., 2017; Cole, 1998; Cole et al., 1998; Grennerat et al., 2012; O'Connor et al., 2020; Wei et al., 2022).

Instruments and techniques have been developed over the years in an attempt to automate this process, which were found to be satisfactory but rarely proliferated outside of the laboratory in which they were created (Eicken, 1993; Lange, 1988; Morgan et al., 1984; Yun and Azuma, 1999). Furthermore, the procedure for the universal stage and analysis of the results have improved markedly since Rigsby first documented the technique (Hansen and Wilen, 2002; Hill and Lasca, 1971; Wilen et al., 2003). Most notably, a device for automated and robust thin section analysis is commercially available (Wilson and Peterzell, 2011) and has been successfully used in various ice applications (Georges et al., 2021; Grennerat et al., 2012; Montagnat et al., 2021). Alternatively, electron backscatter diffraction (EBSD) (e.g. Iliescu et al. (2004); Monz et al. (2021); Seidemann et al. (2020)) is used to determine the *c*-axes—and *a*-axes, which are not discernable from optical methods—of a thin section, though this equipment is highly specialized, requires specially-trained operators, and admits only relatively small ice specimens for analysis.

Also crucial to the discussion of textures and fabrics of ice thin sections is the process of thin sectioning itself. Techniques ranging from rough (hand-melting the ice (Langway, 1958; Shokr and Sinha, 2015)) to refined (double-microtoming method (Shokr and Sinha, 2015; Sinha, 1977)) to something in between (CNC milling) yield different results of thin sectioning which can influence the quality of the surface roughness and thus the image processing of the photographs taken for automated texture and fabric analysis. Presented herein is a method of preparing ice thin sections and analyzing ice textures and quarter fabrics via in-plane photography with any digital camera based on the interference coloration of the ice. Additionally, ice fabrics are simulated with the interference coloration theory which provide a visual reference for ice type identification. Finally, the method is compared with the Rigsby stage technique, sample results are presented, and limitations are identified based on laboratory-grown freshwater ice and ice specimens taken from in the IJsselmeer near Breezanddijk, Netherlands in February 2021.

2. Theory

2.1. Ice birefringence in linearly polarized light

Water ice at standard atmospheric conditions of Earth has hexagonal (1h) crystal structure and, consequently, optically positive uniaxial birefringence (Hobbs, 1974; Pauling, 1935; Petrenko and Whitworth, 1999). While pure freshwater ice is transparent under unpolarized visible light, the shape and orientation of the grains can be readily distinguished to the observer with linearly polarized light because of the birefringence of the ice (see Fig. 1). The birefringence, or double refraction, of ice is weakly dependent on the visible wavelength of light and on temperature above -60°C , and is strongly dependent on the angle between the linearly polarized incident light ray (wave normal) and the *c*-axis, see principal axis of symmetry and the optic axis of the hexagonal crystal (see Fig. 2a) (Bloss, 1961; Hobbs, 1974; Petrenko and Whitworth, 1999; Schulson and Duval, 2009). This double refraction of ice can be described by a refractive index tensor ellipsoid, or indicatrix (see Fig. 2b) (Fueten and Goodchild, 2001; Shestov, 2018).

The angle between the incident light ray (coincident with vertical viewing axis or line of sight (LoS)) and the *c*-axis of an ice crystal can be defined as θ and is typically referred to as inclination angle (Heilbronner and Pauli, 1993), (or sometimes plunge angle (Fueten and Goodchild, 2001) or colatitude angle (Peterzell et al., 2011)). The positive birefringence of ice Δn is defined as the difference between the refractive index of the extraordinary ray and the refractive index of the ordinary ray:

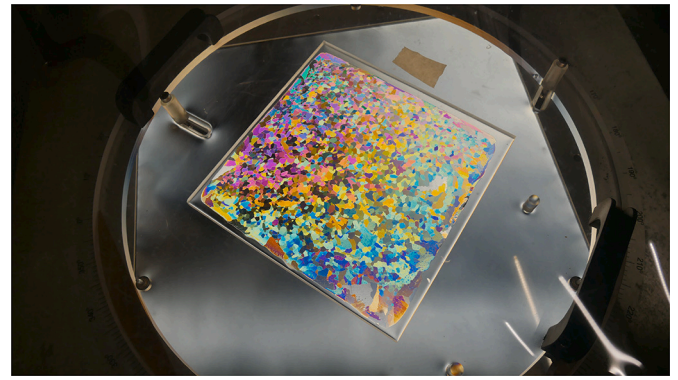


Fig. 1. Oblique photograph of laboratory-grown columnar horizontal ice thin section viewed with crossed-polarized transmitted light in a large polariscope in the ice laboratory at Delft University of Technology. The acrylic plate on which the thin section is welded has dimensions of 220 mm square.

$$\Delta n(\lambda) = n_e(\lambda) - n_o(\lambda) \quad (1)$$

with:

$$n_e(\lambda) = \frac{n_o(\lambda)}{\sqrt{1 + \left(\frac{n_o(\lambda)^2}{n_e(\lambda)^2} - 1\right) \sin^2 \theta}} \quad (2)$$

and:

$$n_o(\lambda) = n_w(\lambda) \quad (3)$$

where λ is the wavelength of the incident light, n_e and n_w are the refractive indices of the extraordinary and ordinary rays, respectively, and n_e and n_o are the refractive indices of the extraordinary and ordinary rays, respectively, that are projected from the indicatrix via inclination angle to the plane orthogonal to the incident ray (see Fig. 2b). The term n_o is constant because the cross section of the indicatrix related to the ordinary ray is circular. The term n_e varies elliptically between n_w and n_e as defined by the indicatrix. The refractive indices of ice as a function of visible light wavelength and temperature (which is treated as constant and about -3°C in this study) are listed in Table A.1. The refractive indices are fit by a Cauchy approximation (Heilbronner and Pauli, 1993):

$$n_{w,e}(\lambda) = A_{w,e} + \frac{B_{w,e}}{\lambda^2} + \frac{C_{w,e}}{\lambda^4} + O(\lambda^4) \quad (4)$$

where a fourth-order approximation is deemed sufficient for the purposes of this study and the corresponding coefficients A , B , and C are fit to the measured data from Table A.1 for n_w and n_e (see Fig. 3). The coefficients for the Cauchy approximations of n_w and n_e of ice and their respective R-squared values as a function of wavelength in nanometers are provided in Table 1.

When an individual ice grain is viewed in a polarization microscope (Heilbronner and Barrett, 2014), polariscope (Pounder, 1965; Shokr and Sinha, 2015), or similar configuration of crossed-polarized transmitted light system, emitted light first passes through the polarizer with nominally north-south (N-S) orientation, which linearly polarizes the light with vertical incident ray (wave normal) and transverse wave parallel to the polarizing (privileged) direction (IR with color purple in Fig. 2c). The linearly polarized light then passes through the ice grain, resolving the light into an ordinary ray (color green in Fig. 2c) and an extraordinary ray (color orange in Fig. 2c) with transverse waves in the plane of the respective n_o and n_e which were projected onto the plane orthogonal to the incident ray. Depending on θ , a difference in the refractive indices means that the extraordinary ray passes through the grain more slowly and results in a retardation, or phase shift, at the exit

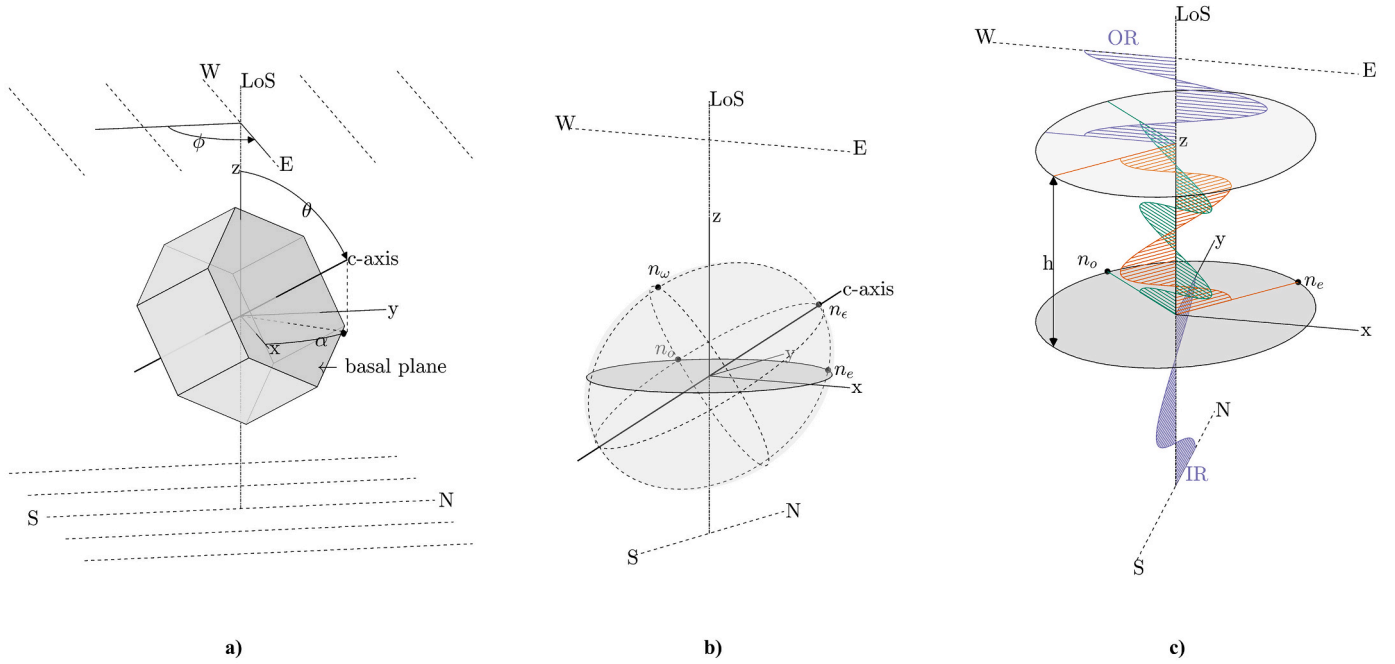


Fig. 2. Diagrams of ice grain specimen between linear polarizers. a) Ice crystal unit cell (orientation of a-axis is arbitrary) with orientation of c-axis (orthogonal to the basal plane) relative to the line of sight (LoS). The c-axis orientation is defined by the inclination angle θ and azimuth angle α relative to the LoS. The angle ϕ between the privileged directions of the N-S polarizer and the W-E polarizer (called the analyzer) is set according to the type of polarization desired. b) Corresponding refractive index tensor ellipsoid of the ice crystal unit cell with refractive indices projected onto the plane orthogonal to the incoming light ray. c) The tensor ellipsoid projected plane with transmission of light rays through the ice of thickness h . The incident ray (IR) is decomposed into the extraordinary ray (color orange) projected onto the c-axis and the ordinary ray (color green) projected orthogonal to the c-axis, and with a path difference caused by the birefringence Δn . The combination of c-axis orientation and ice thickness determine the transmission of the resultant outgoing ray (OR) through the analyzer with orientation $\phi = 90^\circ$ in this case of crossed-polarization ($\theta = 60^\circ$, $\alpha = 45^\circ$, h and light wavelengths not to scale). For more information, refer to, e.g., Bloss (1961) and Shestov (2018). Note that the diagrams are shown at different viewing perspectives for clarity. (For interpretation of the references to color in this figure legend, the reader is referred to the web version of this article.)

Table 1

Coefficients and the R-squared value for the fourth-order Cauchy approximation of the refractive indices of the ordinary and extraordinary rays of ice as a function of light wavelength in nm (see Fig. 3).

	Ordinary	Extraordinary
A	1.2989	1.3002
B	3.7945e+03	3.8042e+03
C	-9.9396e+07	-9.6295e+07
R-squared	0.9984	0.9983

of the grain between the ordinary and extraordinary transverse waves. Thus, elliptically polarized light exits the grain with a resultant transverse wave which reaches the upper polarizer (called the analyzer) with west-east (W-E) privileged direction and may be accepted or rejected depending on whether its components are in that W-E orientation. Finally, the light reaches the receiver (eye, camera, etc.) if the light is accepted by the analyzer.

If no crystal were present, and the angle between the polarizer and analyzer privileged directions ϕ were 90° , then minimum light would pass to the receiver and the image would appear dark. By placing the crystal between the polarizer and analyzer, depending on the orientation of the crystal, interference coloration of the crystal can occur. This is caused by different transmission of the spectral component wavelengths of white light through the analyzer and results in certain colors absorbed and others not (Bloss, 1961; Shestov, 2018). The specific color of a crystal is dependent on Δn (function of θ), thickness of the ice h , angle between polarizer and analyzer ϕ , and the azimuth angle between the polarizer and the c-axis of the crystal α . The intensity of the transmission of the light through the system is defined:

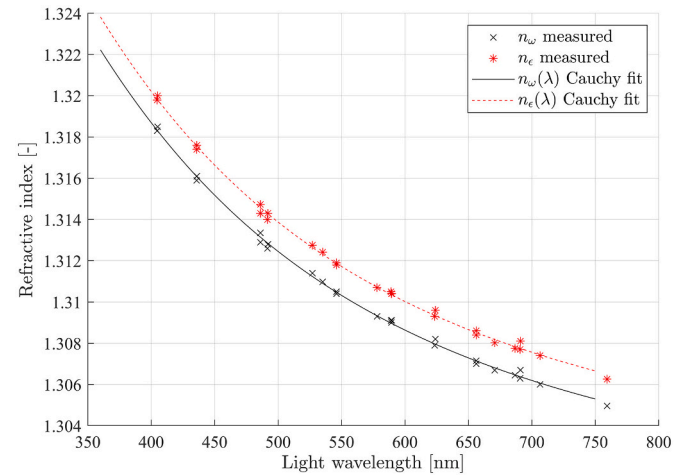


Fig. 3. Measured refractive indices as a function of the wavelength of light for the ordinary and extraordinary rays of ice (Heilbronner and Barrett, 2014; Hobbs, 1974; Petrenko and Whitworth, 1999). The measured values from Table A.1 are fit with a Cauchy approximation (Heilbronner and Pauli, 1993).

$$I = I_0 \cos^2 \phi - \sin 2(\alpha - \phi) \sin(2\alpha) \sin^2 \left(\frac{2\pi h \Delta n}{2\lambda} \right) \quad (5)$$

where I_0 is the incident light intensity (Bloss, 1961; Heilbronner and Pauli, 1993; Price, 1973; Sørensen, 2013). For typical crossed-polarization, $\phi = 90^\circ$, which simplifies Eq. 5 to the following:

$$I|_{\phi=90^\circ} = I_0 \sin^2(2\alpha) \sin^2\left(\frac{2\pi h \Delta n}{2\lambda}\right) \quad (6)$$

which follows [Shestov \(2018\)](#). For a range of h , θ , and α , with $\phi = 90^\circ$, the intensity of transmission of visible light through the system is shown (see [Fig. 4](#)). When the c -axis of the ice crystal is coincident with the incident light ray, $\theta = 0^\circ$, the refractive index of the extraordinary ray equals that of the ordinary ray and the difference, the birefringence, is zero. As a result, the intensity is also zero. The intensity is minimum for $\alpha = 0^\circ$ and increases to maximum for $\alpha = 45^\circ$, but only influences the amplitude and not the proportional shape of the intensity curve over the wavelength spectrum. In other words, α affects the relative brightness of the color of an ice crystal when viewed between crossed polarizers. The color of a crystal is then dependent on h and θ .

The color of an ice crystal, when observed between crossed polarizers, is the combination of the visible light wavelengths that pass through the system, and can be characterized by a quality function ([Shestov, 2018](#)):

$$Q = I_{\max} \left[1 - \int_{\lambda_{\text{violet}}}^{\lambda_{\text{red}}} I \cdot d\lambda / (I_{\max} \cdot (\lambda_{\text{red}} - \lambda_{\text{violet}})) \right] \quad (7)$$

where I_{\max} is the maximum intensity for the range of visible light wavelengths. Note that $\lambda_{\text{violet}} = 350$ nm and $\lambda_{\text{red}} = 750$ nm. This quality function is used in the following section with the interference coloration of ice in crossed-polarized light to demonstrate the coloration of ice grains as a function of c -axis orientation and specimen thickness.

2.2. Interference coloration of ice in crossed-polarized light

The phenomenon of interference colors of birefringent minerals in polarized light is well-established in mineralogy ([Bloss, 1961](#); [Murphy, 2001](#); [Raith et al., 2012](#)). However, digital techniques to accurately represent interferences colors in human vision on computer monitors is an ongoing study ([Linge Johnsen et al., 2018](#); [Sørensen, 2013](#)). With this in mind, the following is an attempt to portray the interference

coloration of ice thin sections. To begin, the intensity from the special case in [Eq. 6](#) is called the spectral color transmission \bar{I}_λ as a vector or matrix and calculated over the range of visible wavelengths of light and expressed as follows ([Sørensen, 2013](#)):

$$\bar{I}_\lambda(h, \theta, \alpha) = \begin{bmatrix} I(\lambda = 350 \text{ nm}, h, \theta, \alpha) \\ \vdots \\ I(\lambda = 750 \text{ nm}, h, \theta, \alpha) \end{bmatrix} \quad (8)$$

where the visible spectrum is considered from 350 nm to 750 nm. The spectral color transmission must be converted from wavelengths of light to red, green, and blue (RGB) channel values for digital displays; this is done with two steps. The first is conversion from spectral color to human vision color with use of the CIE1931 color matching functions ([Stockman et al., 2020](#)):

$$\bar{I}_{XYZ}(h, \theta, \alpha) = \begin{bmatrix} \vec{r}_\lambda \\ \vec{g}_\lambda \\ \vec{b}_\lambda \end{bmatrix} \bar{I}_\lambda(h, \theta, \alpha) = \begin{bmatrix} X \\ Y \\ Z \end{bmatrix} \quad (9)$$

Where \vec{r}_λ , \vec{g}_λ , and \vec{b}_λ are the red, green, and blue sensitivity functions and X , Y , and Z are the human vision color coordinates ([Sørensen, 2013](#)). The second step is conversion from human vision color coordinates to RGB channel values for digital displays. This conversion is done via linear transformation to Adobe RGB ([Pascale, 2003](#)):

$$RGB_{\text{linear}} = M_{RGB} \begin{bmatrix} X \\ Y \\ Z \end{bmatrix} = \begin{bmatrix} R \\ G \\ B \end{bmatrix} \quad (10)$$

with

$$M_{RGB} = \begin{bmatrix} 2.0414 & -0.5649 & -0.3447 \\ -0.9693 & 1.8760 & 0.0416 \\ 0.0134 & -0.1184 & 1.1054 \end{bmatrix} \cdot 10^{-2} \quad (11)$$

Where X , Y , and Z are the red, green, and blue channel values of

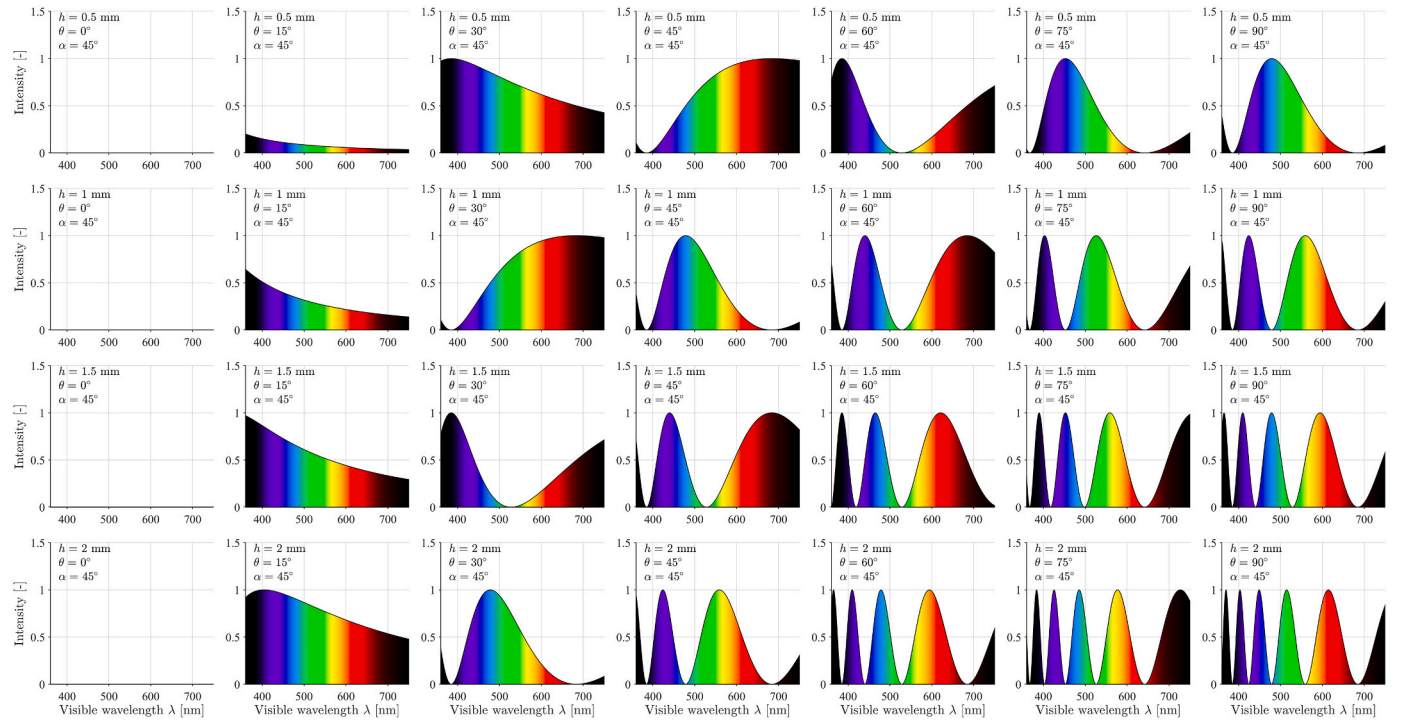


Fig. 4. Intensity of transmission of visible light through the crossed-polarized birefringence light system for ranges of ice thickness h and inclination angle θ , with azimuth angle $\alpha = 45^\circ$ for maximum intensity. Initial intensity I_0 is assumed at unity. The colors for the visible wavelengths of light are converted to RGB values for plotting purposes ([Stockman et al., 2020](#)).

human vision, respectively. Note that there is a typographical error in the first element (row and column 1) of Eq. 6 in Sørensen (2013), which is corrected herein according to page 21 of Pascale (2003). Additionally, the linear transformation matrix M_{RGB} is reduced by two orders of magnitude for RGB channel values between 0 and 1 in MATLAB. However, the linear RGB channel vector RGB_{linear} contains values outside the admissible 0 to 1 range for RGB channel values, which then requires values greater than 1 and less than 0 to be set to 1 and 0, respectively:

$$v_i = \begin{cases} 1, & u_i > 1 \\ 0, & u_i < 0 \\ u_i, & \text{else} \end{cases} \quad \text{for } i = 1, 2, \dots, N \quad (12)$$

where i is an element in RGB_{linear} , v is the clipped RGB channel value, u is the unclipped RGB channel value, and N is the number of elements in RGB_{linear} . Finally, a nonlinear gamma correction is applied to the clipped linear RGB channel vector in accordance with the Adobe RGB 1998 standard (Adobe Systems, 2005):

$$w_i = \begin{cases} v_i^\gamma, & v_i \geq 0 \\ -(-v_i)^\gamma, & v_i < 0 \end{cases} \quad \text{for } i = 1, 2, \dots, N \quad (13)$$

Where w_i is the gamma-corrected, clipped RGB channel value, and $\gamma = 1/2.19921875$. The resulting gamma-corrected, nonlinear RGB channel vector represents the color corresponding to a given ice thickness and c -axis orientation; this result can be populated for ranges of thicknesses, inclination angles, and azimuth angles and plotted with the quality function (see Figs. 5–7). Colors of individual grains can be identified and attributed with known birefringence to the Michel-Lévy color chart or the Raith-Sørensen chart (Raith et al., 2012; Sørensen, 2013). Azimuth and inclination angles of zero result in extinction of the ice crystal as expected since birefringence is zero. For nonzero inclination angle, the azimuth angle controls the brightness, i.e. amplitude, of the given range of colors. For increasing inclination angles from zero to

maximum, the interference colors of the quality function become less monochromatic and more vibrant for the given range of ice thicknesses. For ice thicknesses greater than about 2 mm and for grains with high inclination angles, the colors become more like white light with numerous passes of the wavelengths of light. Practically, this means that c -axis orientations can no longer be distinguished reliably as most or all of the grains possess coloration varying between extinguished dark and grey or white interference coloration.

To summarize the possible interference colors observable for different ice thicknesses, conoscopic interference color patterns are shown in Fig. 8. The interference colors display four-fold symmetry, i.e. 90° degeneracy, meaning that the c -axis of a grain cannot be resolved to its true quadrant in a stereonet in this crossed-polarization system. This limitation is illustrated in Section 2.4 and addressed in Section 5.

2.3. Effect of light source color temperature on interference coloration

While Sørensen (2013) provides a valuable framework by which to visualize interference coloration on digital displays, their approach ignores a fundamental component: color temperature of the light source (Linge Johnsen et al., 2018). The color temperature influences the light source spectral distribution; this light source color temperature can be determined when the light is assumed to originate from a black body irradiator as monochromatic irradiance or emissive power [W m^{-3}] (Forsberg, 2021):

$$E_{b\lambda} = \frac{C_1 \lambda^{-5}}{e^{\frac{C_2}{\lambda T_c}} - 1} \quad (14)$$

where constant $C_1 = 3.74 \times 10^{-16} \text{ W m}^2$, constant $C_2 = 1.4388 \times 10^{-2} \text{ m K}$, and color temperature T_c is in units of Kelvin. In adjusting the interference colors based on the color temperature of the light source, Eq. 9 is altered as follows (Linge Johnsen et al., 2018):

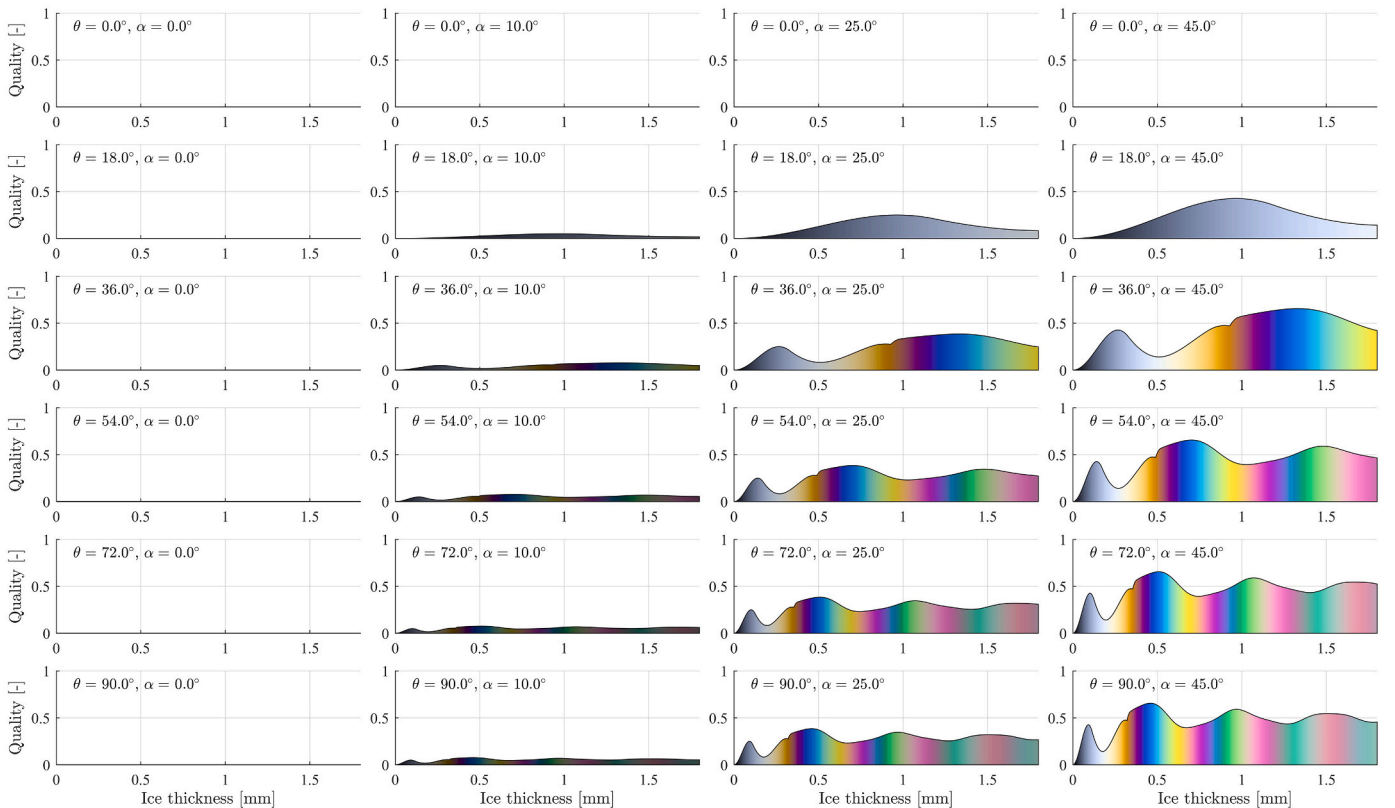


Fig. 5. Interference colors from the quality function that are transmitted by the birefringence system, for a range of inclination angles and azimuth angles, as a function of ice thickness.

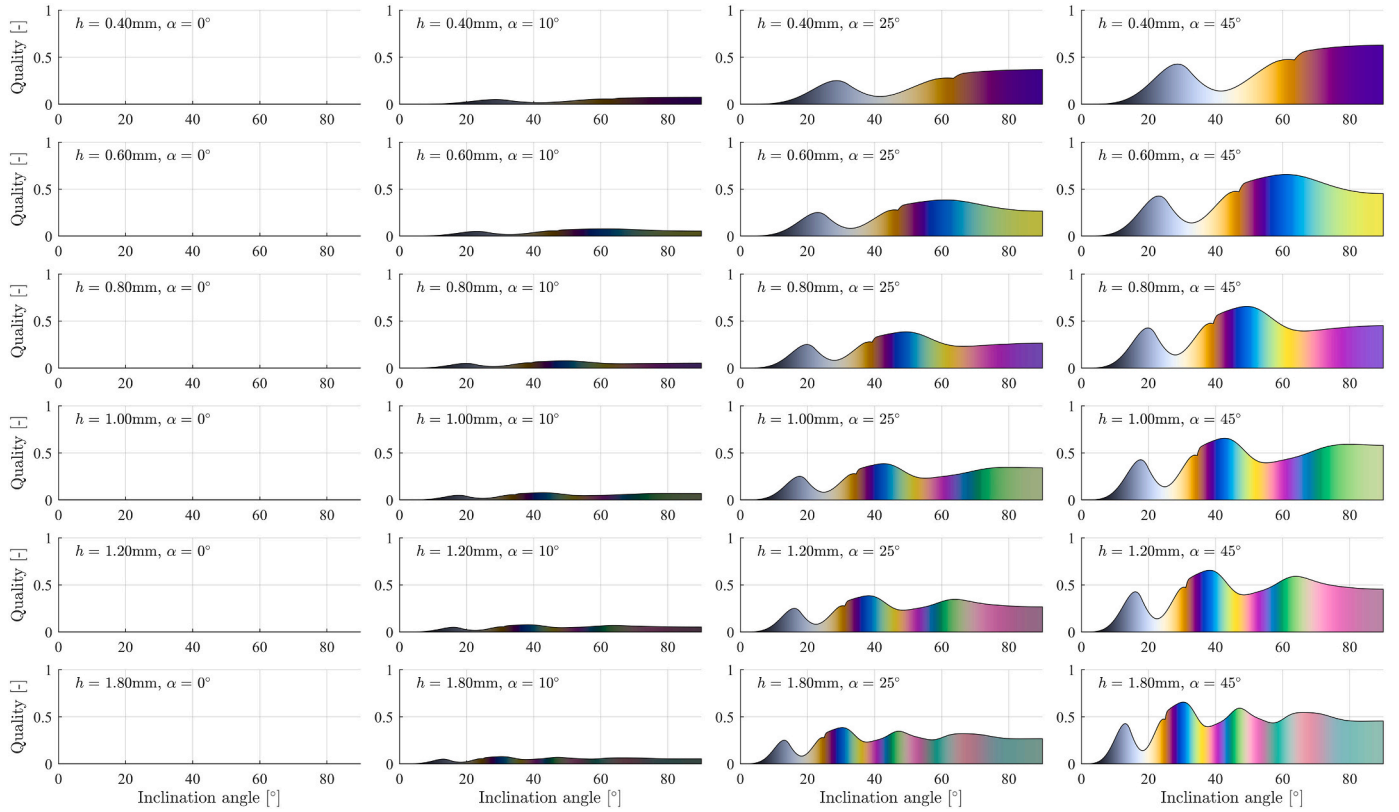


Fig. 6. Interference colors from the quality function that are transmitted by the birefringence system, for a range of ice thicknesses and azimuth angles, as a function of inclination angle.

$$\begin{aligned} \bar{J}_{XYZ} &= \begin{bmatrix} \vec{r}_\lambda \\ \vec{g}_\lambda \\ \vec{b}_\lambda \end{bmatrix} (\widehat{E}_{b\lambda} \odot \bar{I}_\lambda(h, \theta, \alpha)) \\ &= \begin{bmatrix} \vec{r}_\lambda \\ \vec{g}_\lambda \\ \vec{b}_\lambda \end{bmatrix} \left(\begin{bmatrix} \widehat{E}_{b\lambda}(\lambda = 350 \text{ nm}, T_{cLS}) \\ \vdots \\ \widehat{E}_{b\lambda}(\lambda = 750 \text{ nm}, T_{cLS}) \end{bmatrix} \odot \bar{I}_\lambda(h, \theta, \alpha) \right) \end{aligned} \quad (15)$$

where $\widehat{E}_{b\lambda}$ is the monochromatic irradiance spectrum vector of the light source normalized by its maximum value over the spectrum, operator \odot is the Hadamard (element-wise) product, and T_{cLS} is the light source color temperature. The application of Eq. 15 to the previous procedure to obtain the interference colors will result in colors that have a white-balance shift in color temperature. To adjust interference coloration from a light source with a warm or cool color temperature to interference coloration with white balance or other color temperature, a transformation is performed by using the light source color temperature and a target color temperature. This procedure is called chromatic adaptation and is done with the following manipulations:

$$\bar{W}_{XYZ}(T_{cLS}) = M_A \begin{bmatrix} \vec{r}_\lambda \\ \vec{g}_\lambda \\ \vec{b}_\lambda \end{bmatrix} \widehat{E}_{b\lambda}(T_{cLS}) \quad (16)$$

and

$$\bar{W}_{XYZ}(T_{cTg}) = M_A \begin{bmatrix} \vec{r}_\lambda \\ \vec{g}_\lambda \\ \vec{b}_\lambda \end{bmatrix} \widehat{E}_{b\lambda}(T_{cTg}) \quad (17)$$

with

$$M_A = \begin{bmatrix} 0.8951 & 0.2664 & -0.1614 \\ -0.7502 & 1.7135 & 0.0367 \\ 0.0389 & -0.0685 & 1.0296 \end{bmatrix} \quad (18)$$

Where T_{cTg} is the target color temperature and M_A is the linearized Bradford matrix (Linge Johnsen et al., 2018; Pascale, 2003). Next, the chromatic adaptation transformation matrix is constructed:

$$M_{CA} = M_A^{-1} \text{diag}(\bar{W}_{XYZ}(T_{cTg}) \odot \bar{W}_{XYZ}(T_{cLS})^{-1}) M_A \quad (19)$$

where $\text{diag}(\bullet)$ is the diagonalization operator. Finally, the light-sourced modified human color vision matrix \bar{J}_{XYZ} is chromatically adapted:

$$\bar{J}_{XYZca} = M_{CA} \bar{J}_{XYZ} \quad (20)$$

where this chromatically adapted matrix can then be used in Eq. 10–13 as previously explained. An example of chromatic adaptation is presented in the next section. Note that, unless otherwise stated, all simulated interference colors in the present study are rendered at a color temperature of 6504 K.

2.4. Multi-level Voronoi tessellation for simulated ice fabrics

By using interference colorations and Voronoi tessellation (dual graph of Delaunay triangulation), representative thin sections of ice textures (or fabrics) can be artificially generated. However, the representative grains generated by Voronoi tessellation do not follow any grain growth behavior expected during ice cover formation. As a compromise between conventional Voronoi tessellation and grain growth simulation based on thermodynamics and geometric constraints, an ad hoc multi-level Voronoi tessellation is implemented (Yadegari et al., 2014). An example simulated thin section is shown in Fig. 9 with a polar plot of the orientation of the *c*-axes and their respective

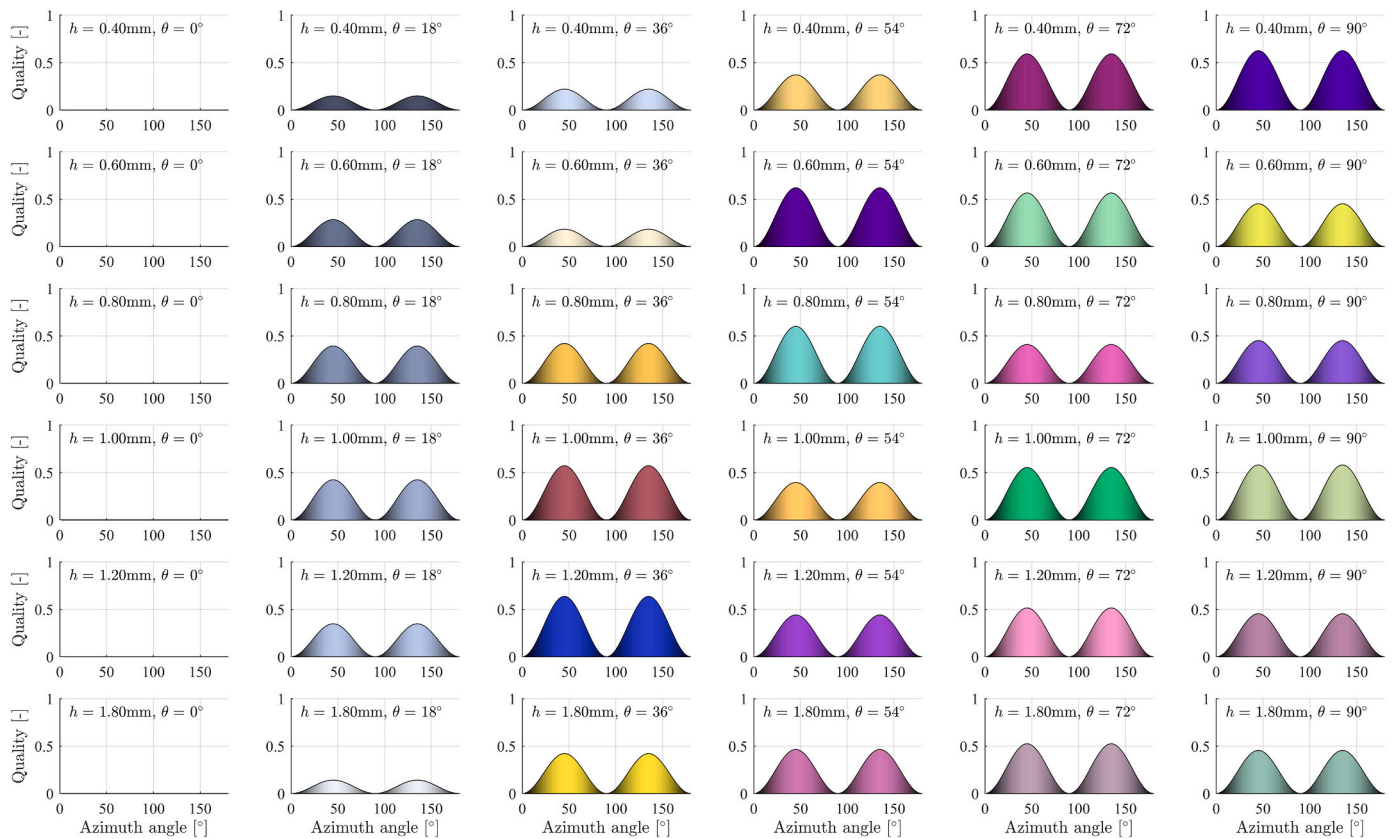


Fig. 7. Interference colors from the quality function that are transmitted by the birefringence system, for a range of ice thicknesses and inclination angles, as a function of azimuth angle.

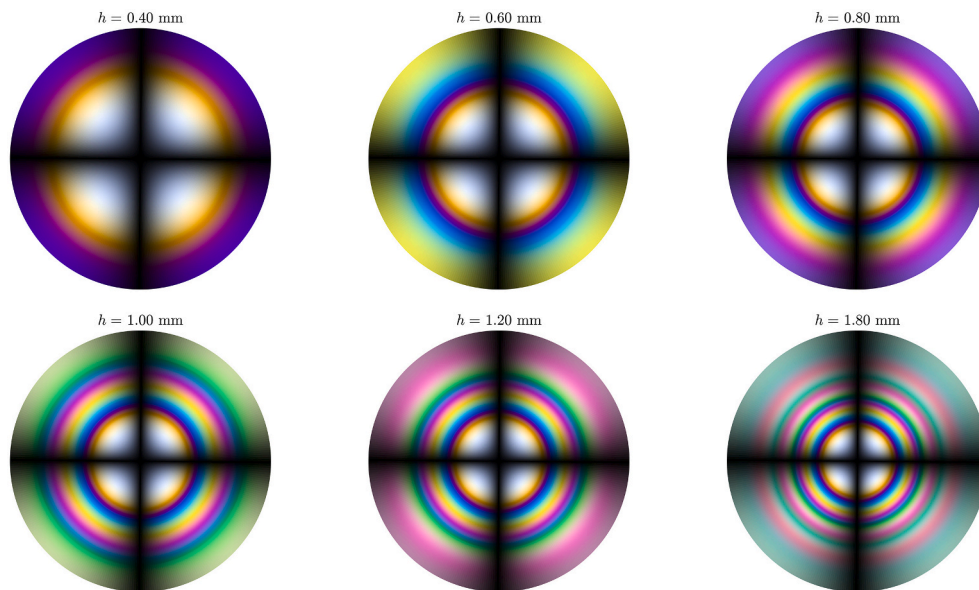


Fig. 8. Conoscopic interference color patterns, for a range of ice thicknesses, as a function of azimuth and inclination angles. Note that the LoS is coincident with the center of the conoscopic interference color pattern.

interference color at initial specimen orientation. Extinction angles can be seen around inclination angles of zero and azimuth angles collinear with the privileged directions of the polarizer (N-S) and analyzer (W-E), as viewed in the polar plot (note the four-fold symmetry of the interference colors). This ice fabric is roughly representative of a medium-diameter-grained granular or columnar horizontal thin section with

random c-axis orientations as observed in ice types P2–P4 and S2, S4, S5, and T1–T3 (Michel and Ramseier, 1971). For freshwater columnar and first-year sea ice immediately below the transition layer (e.g. Schwarz and Weeks (1977)), type S2 ice is observed and would appear with a distribution of colors such as in Fig. 10. It is clear that c-axes randomly oriented in the plane of the thin section would display roughly one or

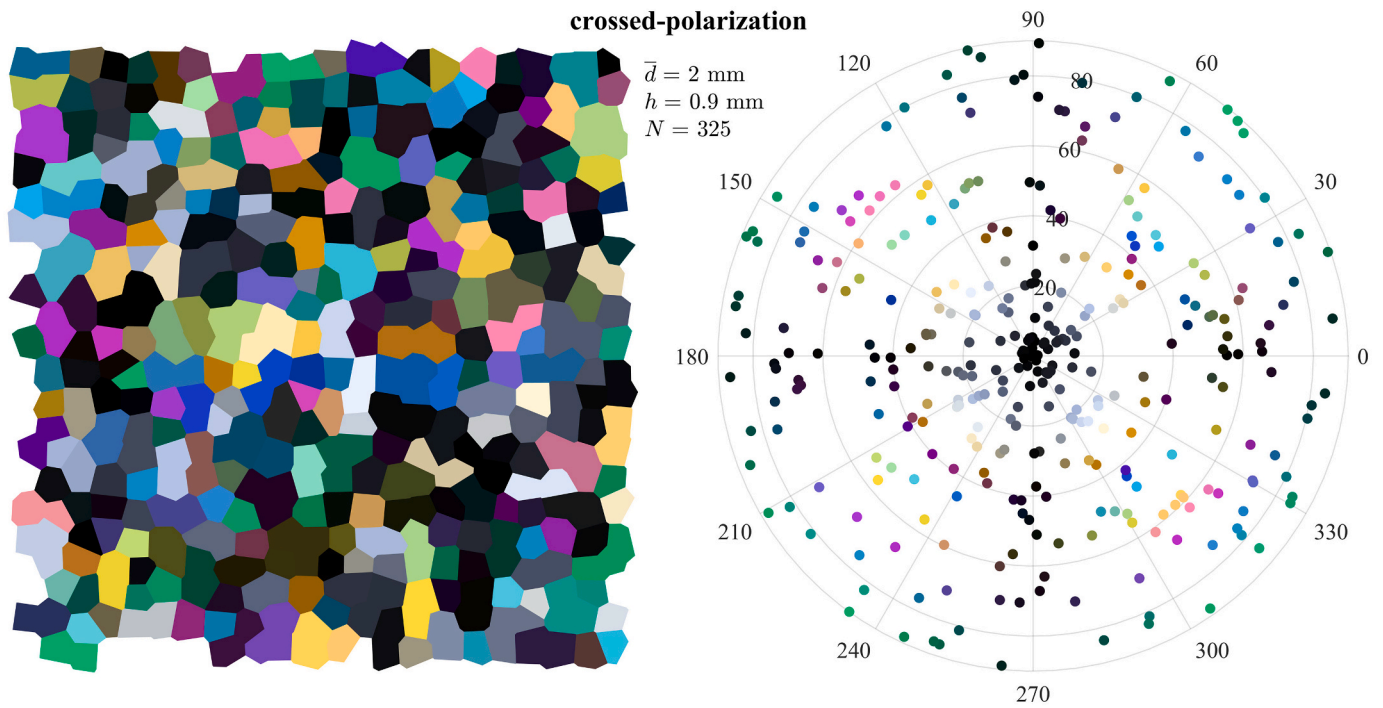


Fig. 9. Left: Example multi-level Voronoi diagram of representative, simulated ice fabric in crossed-polarized backlighting with thickness h , and with quantity N ice grains of uniformly distributed size with arbitrary top-level diameter \bar{d} . Right: polar plot with interference-colored points of inclination (radial) and azimuth (circumferential) angles in degrees as defined for each of the ice grains.

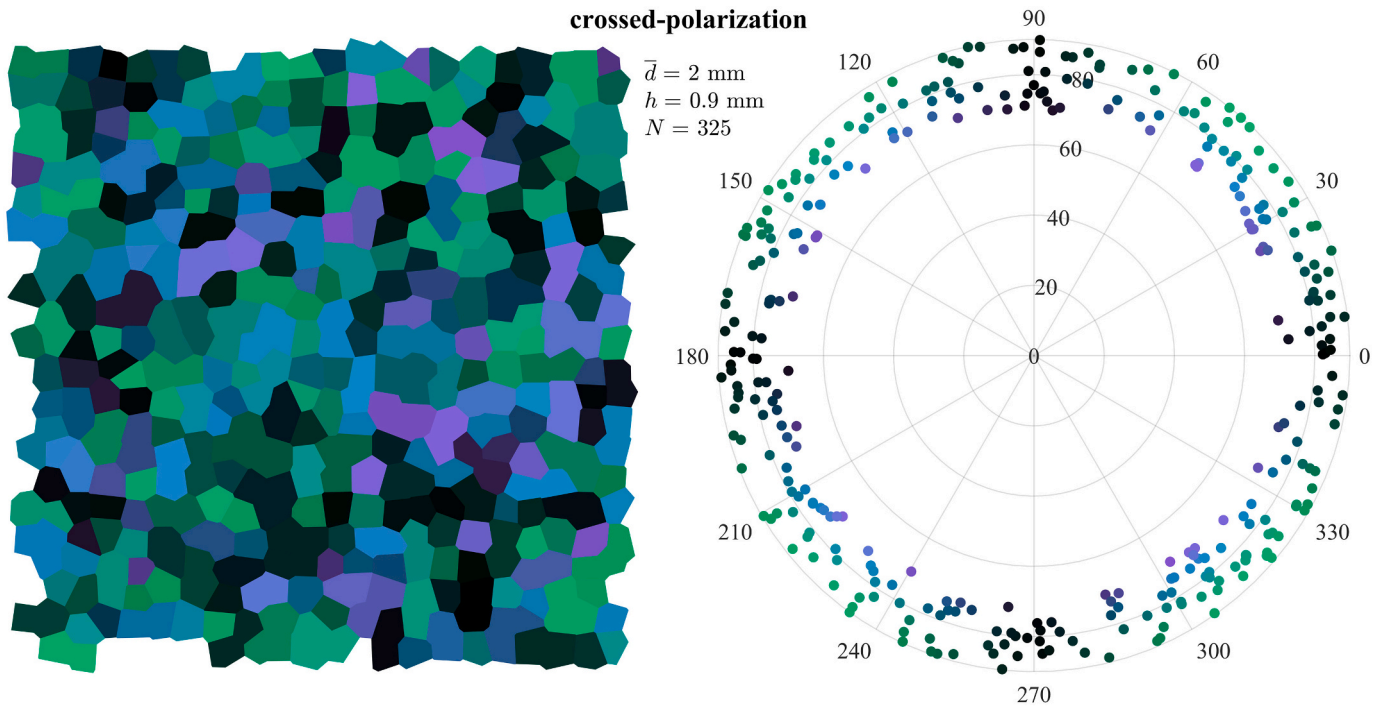


Fig. 10. Left: Example multi-level Voronoi diagram of representative, simulated ice fabric of S2 type ($\theta = 80 \pm 10^\circ$) in crossed-polarized backlighting with thickness h , and with quantity N ice grains with arbitrary top-level diameter \bar{d} . Right: polar plot with interference-colored points of inclination (radial) and azimuth (circumferential) angles in degrees as defined for each of the ice grains.

two colors with a range of brightness between those respective colors and extinction. This approach can also be used to examine the effect of light source color temperature without chromatic adaptation on the interference coloration of the grains, in this case the effect on S2 type ice (see Fig. 11).

3. Methodology

There are two main approaches to collecting photographs of ice thin sections for quantitative analysis. First and most commonly, an ice thin section is placed between stationary, crossed-polarizers and

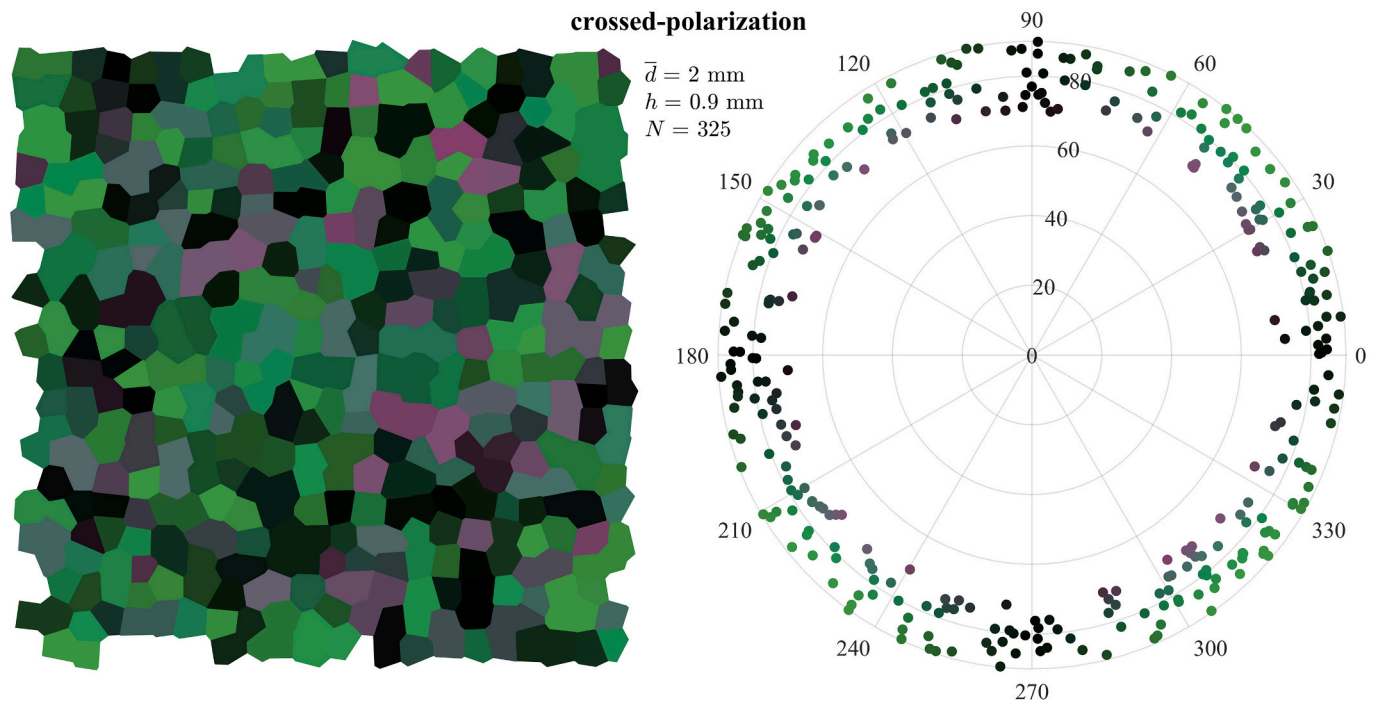


Fig. 11. The Voronoi diagram and polar plot from Fig. 10 with a light source color temperature of 3200 K and without chromatic adaptation (equivalent to chromatic adaptation with target color temperature of 3200 K).

photographs are taken of the ice as the thin section is rotated azimuthally. While this technique is easy to implement, it has serious implications for image registration. First, if the line of sight is not coincident with the axis of azimuthal rotation, then eccentricity of the thin section in the image will occur. When the images are to be registered, or transformed such that all of the images contain the same orientation of the thin section, this eccentricity needs to be eliminated. Additionally, if the thin section is rotated without a fixed axis of rotation, then accidental translations can occur which also need to be eliminated. Second and ideally, image registration can be avoided altogether by having the thin section be stationary and, instead, rotating the crossed polarizers while maintaining their perpendicular privileged orientation. This procedure permits pixel-to-pixel image correspondence for precise image comparison, but requires special equipment for synchronous rotation of the crossed-polarizers. For the present study, the former technique is available and thus image registration is required for pre-processing the images for quantitative analysis. Moreover, being most common, this method is most useful to be explained for others to use for field and laboratory work.

3.1. Image registration

In the field of image processing, image registration refers to the process of transforming one image such that the result optimally matches a reference or target image. The transformations can include but are not limited to translation, rotation, and shear. When registering a series of images, called an image stack, one image is selected as a reference image to which all other images of the stack are registered. For image registration of the rotation of a thin section between crossed-polarizers, it is obvious that the rotation needs to be registered. But if there is an eccentricity in the axis of rotation of the thin section, or the thin section accidentally translates during rotation, then these translations need to be registered as well. Distortions in the image as a result of misalignment of the camera with the plane of rotation can occur as well, which require shear transformations to be registered. In all, simply reversing the rotations of the images may not suffice to properly register the image stack. Note again that if the crossed-polarizers are rotated

about a stationary thin section, then image registration is not necessary. Image registration can be performed with photographs taken in either parallel- or crossed-polarized backlighting; it is recommended that photographs are taken under both conditions. Certain ice types may prove to be more challenging to register (e.g. horizontal section of S1 type ice) with crossed-polarization and thus easier to register in parallel-polarization.

3.2. Grain boundary segmentation

Once the photographs have been taken and the images have been registered if necessary, the registered image stack is chromatically adapted to 6504 K using the *chromadapt* function in MATLAB, and then can be processed to identify the grain boundaries via segmentation. This allows for identification of individual grains within which the pixels can be attributed to that particular grain from each photograph. While many different methods and approaches exist (Eicken, 1993; Gay and Weiss, 1999; Goodchild and Fueten, 1998), the following procedure was found to be most reliable for several ice types. Explanation for the image processing techniques can be found in literature (Gonzalez and Woods, 2008; Heilbronner and Barrett, 2014). First, for each image in the image stack, the image is divided into its component RGB channels (monochromatic versions of the colored image from the red, green, and blue channels). For each of these greyscale images, a Sobel filter is applied with a heuristically-determined threshold which is then scaled ad hoc. All greyscale images are then combined via Boolean multiplication. This combined image is then subjected to the following morphological operations. First, a majority neighborhood morphological operation is performed. Second, a morphological closing with a 3×3 square kernel is done. Third, the image is morphologically skeletonized. Fourth, the image is morphologically de-spurred. Finally, the image is morphologically cleaned. The boundaries of grains can then be traced using the Moore-Neighbor tracing algorithm modified by the Jacob's stopping criteria (*bwboundaries* function in MATLAB).

Regions are defined by the closed boundaries, from which the number of pixels inside each region and the shape of the boundary can be determined. Using this information and a scale in one of the reference

images, the grain area, centroid, equivalent diameter, and other characteristics can be calculated. This approach is clearly more user-friendly and less biased than the manual linear intercept method commonly referred to in literature (Durand et al., 2006; Snyder et al., 2015). These regions each define the set of pixels from the image stack which are used to determine the extinction of the *c*-axis of the grain in the azimuth and the color at brightest to be used for approximating the inclination angle. This is discussed in the next sections.

3.3. Grain azimuth extinction and orientation of brightest color

As the image stack is the set of registered photographs which have been rotated in the azimuth by at least 90°, the variation in the intensity of each grain should expose the undulose extinction if the *c*-axis is not collinear with the LoS. This done by finding image with the azimuth angle resulting in the minimum color distance in the RGB color space of the color image stack for each grain, as defined by its region from the grain boundary segmentation. The color distance U_{RGB} is found as follows:

$$U_{RGB} = \sqrt{R^2 + G^2 + B^2} \quad (21)$$

which is the Euclidean distance in the RGB color space. Conversely, the color of each grain at its highest intensity, when $\alpha \approx 45^\circ$, can be confirmed as 45° from the extinction angle by finding the image with the azimuth angle resulting in the maximum color distance of the color image stack. This manner only finds azimuth angle of the *c*-axis in one quadrant of its four-fold symmetry, which cannot be distinguished with crossed-polarized light (see Fig. 8). Important to note is the issue of deciding on a color representative of the entire grain, based on the collection of pixels in each grain. Statistical values of mean, median, mode, and maximum brightness or minimum extinction coloration are considered. The median of the color is chosen as representative for the entire grain for the analysis in Section 4.

3.4. Grain inclination angle

To determine the inclination angle in this case of azimuth rotation of the thin section only, an attempt was made to compare the interference color of each grain at its brightest with a look-up table based on the theory from Section 2. For a known thickness and azimuth angle, the color of the grain can be compared with a look-up table of colors associated with the range of inclination angles possible for the grain (e.g., see Figs. 6 and 8). The inclination angle is selected based on the minimum color difference between the color of the grain and the interference colors of the look-up table. The minimum color difference is computed in the L*a*b* color space using MATLAB function *imcolordiff* based on the CIE94 standard (e.g. Melgosa (2000)).

3.5. ColorIce MATLAB toolbox

The *ColorIce* toolbox of programs for registering the image stack, segmenting the grain boundaries, and generating ice texture and quarter fabric diagrams is written in MATLAB version 2021a and publically available for use at the following link: <https://doi.org/10.4121/19824067.v1>.

4. Application

The theory and tool are applied in three parts to demonstrate the advantages and limitations of the proposed method. The first is a comparison, conducted in the ice laboratory at the Norwegian University of Science and Technology, between the Rigsby stage technique and *ColorIce* using freshwater laboratory-grown ice. The second is the implementation of *ColorIce* for a large horizontal thin section of freshwater laboratory-grown ice which was grown in the ice laboratory at Delft

University of Technology. Finally, the third part entails application of *ColorIce* to a series of horizontal sections of an ice core taken from the IJsselmeer near Breezanddijk, Netherlands in February 2021.

4.1. Validation against Rigsby stage technique

Freshwater ice was prepared at the ice laboratory at the Norwegian University of Science and Technology using the following techniques. First, Trondheim tap water at about 20°C was poured into a cooler. The water was cooled at −12°C until a thin ice surface forms, after which the ice was removed and the surface was dry-seeded with crushed ice sieved to less than 2 mm diameter. The ice was left to grow to about 120 mm, after which the ice was removed from the cooler by cutting the ice with a saw. An ice plate was cut from the ice block with a band saw to approximately 80 by 80 by 3 mm. The ice plate was polished by hand until smooth, welded to a glass plate with warm tap water, and reduced to below 1 mm with a sledge microtome equipped with vacuum pump. The thin section was placed in the Rigsby stage and a series of photographs were taken of the specimen while incrementally rotating the thin section through the azimuth by 90°.

The Rigsby stage technique (Langway, 1958; Weeks and Hibler III, 2010; Wilen et al., 2003), with corrections for refraction (Kamb, 1962; Wilen, 2000), was applied to two horizontal thin sections of the seeded, freshwater columnar ice, and for each thin section 30 grains were selected and their *c*-axes were determined thrice. While the reported error of the Rigsby stage technique is 5° (Iliescu et al., 2004; Langway, 1958), it was found in the present study that the mean standard deviation of the error in the inclination angles was 5.4°. Additionally, the azimuth angle for a given *c*-axis was found to occasionally vary significantly due to sensitivity in judgment as to which quadrant the *c*-axis was located based on the manipulations of the out-of-plane axes of the stage; thus, the median of the azimuth angle for each grain was chosen as representative. The results from the Rigsby stage technique were then compared with the results from *ColorIce*. Because of the four-fold symmetry inherent in conoscopic crossed-polarization used in *ColorIce*, the fabrics from the Rigsby stage technique were rotated into one quadrant for valid comparison. The inclination angles were compared directly, but the azimuth angles were compared to the minimum difference with either α or $90^\circ - \alpha$ because the complements of the angles cannot be distinguished in *ColorIce*. The mean (standard deviation in) difference in inclination and azimuth angles were found to be 11.5° (8.0°) and 2.9° (1.0°), respectively. Assuming a normal distribution in human error, these errors are comparable to those of the Rigsby stage technique and are deemed suitable for characterizing ice quarter fabrics.

4.2. Laboratory-grown freshwater ice

Freshwater ice was prepared at the ice laboratory at Delft University of Technology using the following techniques. First, Delft tap water at about 20°C was poured into a cooler retrofitted with a heated pressure-relief pipe connected to the bottom of the cooler. The water is cooled at −20°C until a thin ice surface forms, after which the ice is removed and the surface is dry-seeded with crushed ice sieved to less than 2 mm diameter. The ice is left to grow to about 50 or 100 mm, after which the ice is removed by first draining the water from the cooler via a ball valve on the pressure-relief pipe and then cutting the ice from the box with a saw. The ice block is cut with a band saw to approximately 200 by 200 by 10 mm. Either this ice plate is used to seed another ice growth cycle by replacing the crushed ice (Barrette et al., 1993), or the ice plate is directly used in the following manner. The ice plate is welded to an acrylic plate with warm tap water and milled level with a CNC machine. The ice plate is then removed from the acrylic and the milled surface is polished by slight melting with a hair dryer and welded to the acrylic. The ice plate is finally milled to a target thickness of 0.30 ± 0.15 mm. The thin section on the acrylic plate is placed in a polariscope and photographs are taken while incrementally rotating the thin section

through the azimuth by 90° .

An example result of the method from Section 3 applied to a horizontal thin section of freshwater columnar ice is shown in Fig. 12. The c-axes are not strictly in the horizontal plane but are randomly oriented in the range measured for the quarter fabric. Generally, the majority of the c-axes lie between 45° and 90° from the LoS. The accuracy of the azimuth angle is estimated at $<5^\circ$ because the azimuth increments of the photographs were taken every 5° ; more photographs at smaller angle increments (e.g. every 2° for a total of 44 photographs, with an accuracy of $<2^\circ$) increases the azimuth accuracy. The mean equivalent grain diameter is 10.1 mm with the largest segmented grain of around 30 mm diameter. The median of the color is chosen as statistically representative of the color within a grain at brightest azimuth angle, and is applied to the point in the corresponding polar plot.

Ideally, the colors in the polar plot should approximately match those of the interference colors as a function of inclination angle as seen in Figs. 6 and 8. However, since the thickness varies across the section by

an amount significant enough to change the interference color, the colors are then overlapping due to their dependence on both the inclination angle and on the thickness differences. This variation is compensated by inputting a measured thickness field (accuracy of ± 0.10 mm) into the method such that the inclination angles are determined with a specific thickness at the centroid of each segmented grain which should be representative of the true thickness of the specimen and the corresponding interference color at that location.

4.3. IJsselmeer lake ice

Cores of 90 mm diameter were drilled from landfast ice (salinity of <1 ppt) which formed near Breezanddijk, Netherlands in the IJsselmeer. Analysis of two horizontal thin sections from the same core are provided, the first from about 20 mm from the ice cover surface (see Fig. 13), and the second from about 50 mm from the surface (see Fig. 14). The 20 mm-depth thin section displays grains with c-axes

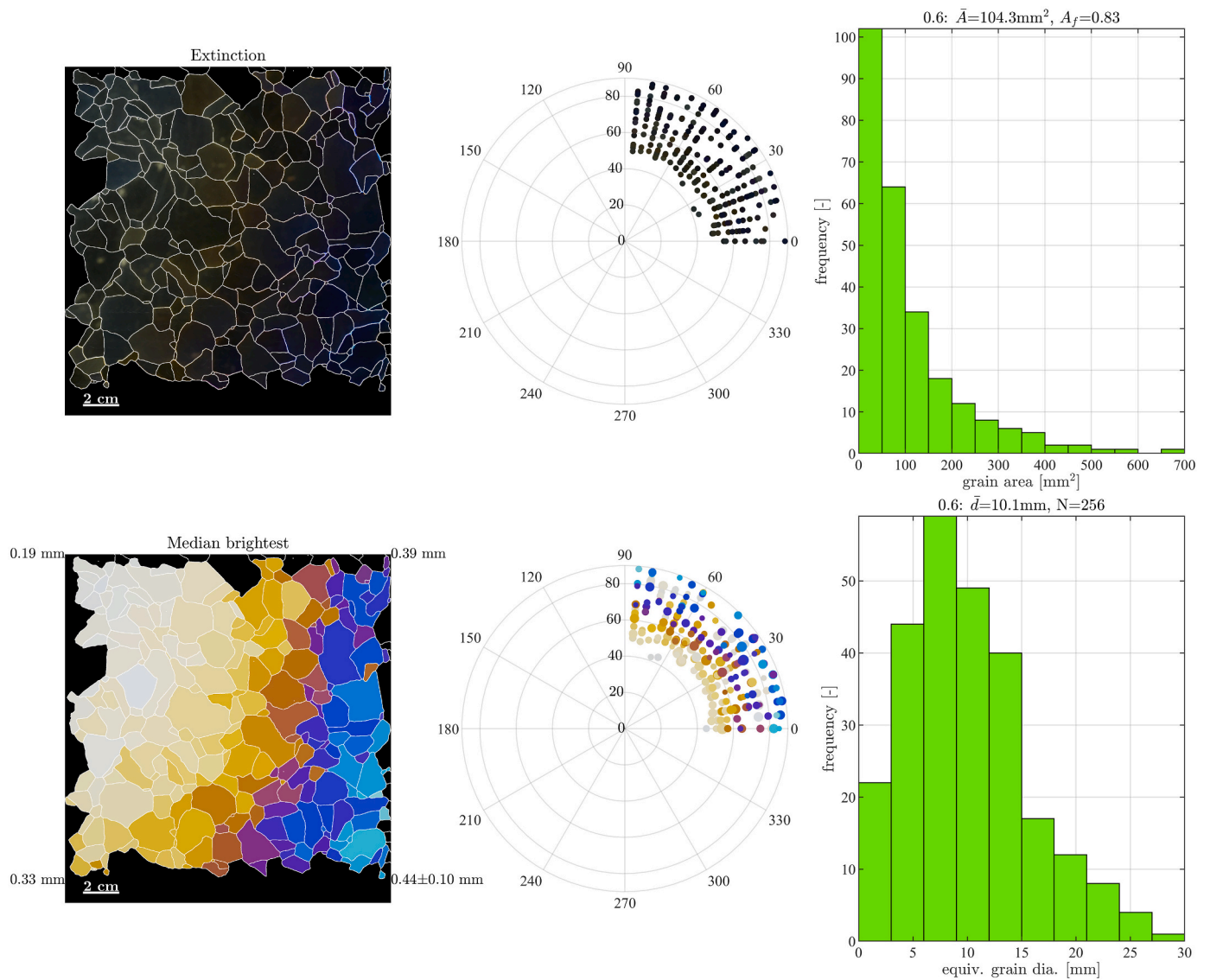


Fig. 12. Analysis of horizontal thin section of freshwater columnar ice. Left column: composite of extinct grains at their respective extinction angles and composite of median value of brightest color of each grain. Center column: corresponding polar plots for the extinction and brightest median values of the c-axes of the grains, with the colored points scaled with grain size. Right column: distribution of grain areas and equivalent grain diameters, with mean grain area \bar{A} , area fraction analyzed of the total image area A_f , mean equivalent grain diameter \bar{d} , and number of grains analyzed N . 18 photographs were taken with 5° azimuth increments. Each registered image has 1863 by 1863 pixels, and the analyzed grains are superimposed onto the original image without azimuth rotation. The ice thicknesses and tolerance are specified at the corners of the median brightest composite image. A light source color temperature of 4000 K and chromatic adaptation to 6504 K were used.

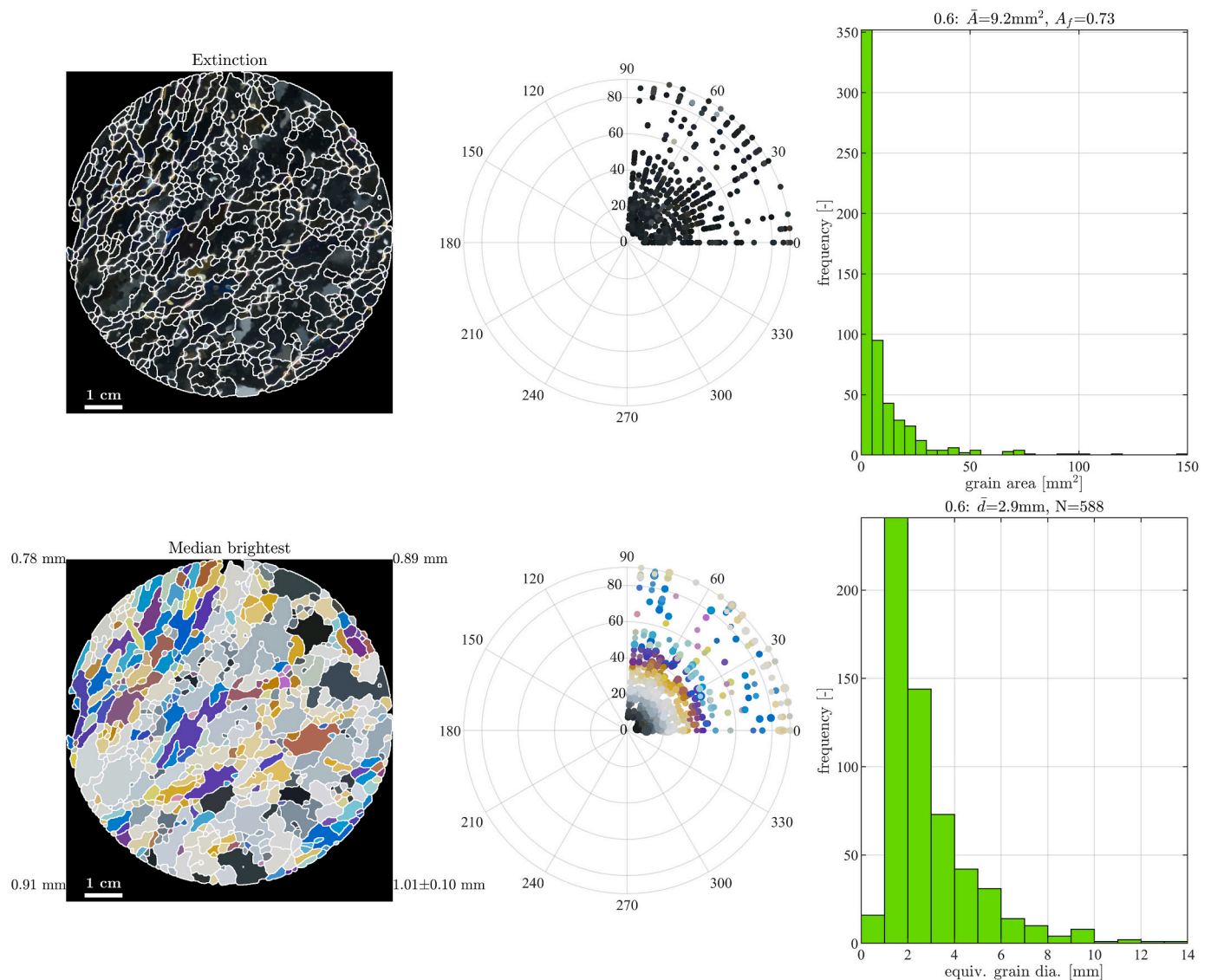


Fig. 13. Analysis of horizontal thin section of IJsselmeer ice taken from about 20 mm from the ice cover surface. Left column: composite of extinct grains at their respective extinction angles and composite of mode value of brightest color of each grain. Center column: corresponding polar plots for the extinction and brightest median values of the c -axes of the grains, with the colored points scaled with grain size. Right column: distribution of grain areas and equivalent grain diameters, with mean grain area \bar{A} , area fraction analyzed of the total image area A_f , mean equivalent grain diameter \bar{d} , and number of grains analyzed N . 18 photographs were taken with 5° azimuth increments. Each registered image has 870 by 870 pixels, and the analyzed grains are superimposed onto the original image without azimuth rotation. The ice thicknesses and tolerance are specified at the corners of the median brightest composite image. A light source color temperature of 4000 K and chromatic adaptation to 6504 K were used.

clustered towards nearly vertical, low inclination angles, which then tend to transition to higher inclination angles with depth in the 50 mm-depth thin section. The azimuth angles of the c -axes show some preferential orientation around 45° at 50 mm-depth.

5. Discussion

The *ColorIce* tool provides a method from which further developments can be made for assessment of ice microstructure. The analysis can be applied to individual photographs for preliminary grain boundary segmentation and ice texture analysis, as well as to image stacks of photographs of thin sections rotated between polarizers for complete texture analysis and quarter fabrics. For the present study, a large polariscope, a Rigsby stage, and a PANASONIC LUMIX DMC-GX80 digital camera (16 megapixel sensor) with a PANASONIC MFT 12–32 mm F/3.5–5.6 lens were used, but the method permits any crossed-

polarization transmitted light system setup and any digital camera with a lens that adequately captures the thin section in focus.

5.1. Rigsby stage technique

While the Rigsby stage technique reveals the c -axis orientations of the grains within the full four quadrants of the stereonet, this method does not yield the ice texture. The *ColorIce* tool, at the very least, is compatible with universal stages and provides ice textures and quarter fabrics for initial study. In other words, the *ColorIce* tool supplements universal stage techniques with ice textures and offers fabric information when universal stages and other specialized equipment are not available.

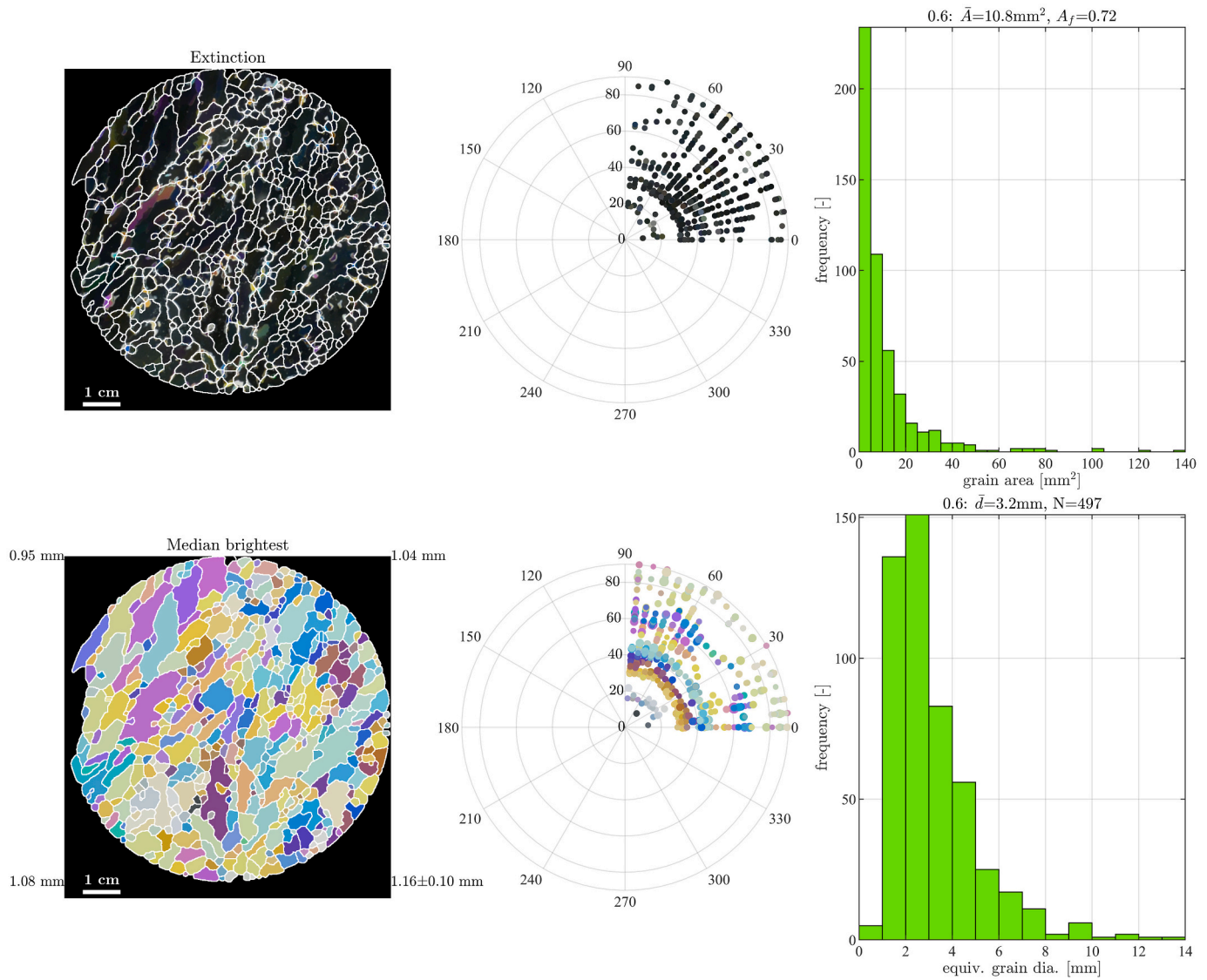


Fig. 14. Analysis of horizontal thin section of IJsselmeer ice taken from about 50 mm from the ice cover surface. Left column: composite of extinct grains at their respective extinction angles and composite of mode value of brightest color of each grain. Center column: corresponding polar plots for the extinction and brightest median values of the c -axes of the grains, with the colored points scaled with grain size. Right column: distribution of grain areas and equivalent grain diameters, with mean grain area \bar{A} , area fraction analyzed of the total image area A_f , mean equivalent grain diameter \bar{d} , and number of grains analyzed N . 18 photographs were taken with 5° azimuth increments. Each registered image has 872 by 872 pixels, and the analyzed grains are superimposed onto the original image without azimuth rotation. The ice thicknesses and tolerance are specified at the corners of the median brightest composite image. A light source color temperature of 4000 K and chromatic adaptation to 6504 K were used.

5.2. Limitations

As made clear by the polar plots in Figs. 12–14, the quarter fabric contains c -axes with orientations only between 0° and 90° in the azimuth. This is due to the four-fold symmetry of the interference coloration theory (see Fig. 8). More photographs of the thin sections from 90° to 180° in the azimuth would result in a repetition of the results in each of the four quadrants. This observation does not affect e.g. relative misorientation angles between the grains within the 90° degeneracy, but does limit results when exact c -axis orientation are required for applications such as the Schmid factor.

Another limitation of automatic grain boundary segmentation is the lack of a ground truth of the image stack. The grain boundaries can be generally identified visually by an observer based on the gradient between any two grains of sufficiently different interference colors, but this does not mean there is a known solution apart from manually mapping the grain boundaries. Therefore, any result from the automatic

grain boundary analysis must be deemed acceptable by the user. Regardless of the subjectivity of the user, the results are more quantitatively tractable than simply providing a photograph of an ice thin section without any statistical measure of grain boundaries, shapes, areas, or equivalent diameters.

When color-matching in the comparison with the Rigsby stage technique, it was found that in some cases the inclination angles deviated significantly (see Fig. 15). Due to the similarity of some interference colors as a function of inclination angle (see Fig. 6), the color matching fails to identify the correct inclination angle. In this particular case, the gold color around 35° resulted in a global minimum instead of the yellow color around 60° .

The algorithms applied in the present analysis do not address the effects of cracks or impurities such as air pockets on the identification of grain boundaries and interference colors. This issue requires further development, likely incorporating manual or user-interactive intervention in the image processing techniques described previously. One of the

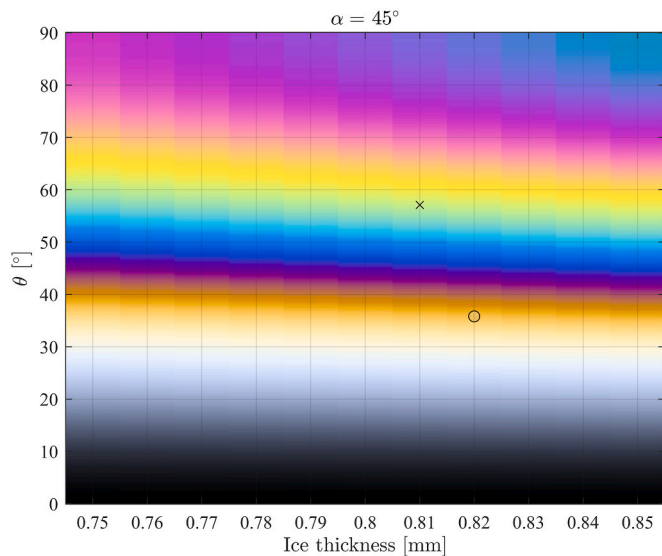


Fig. 15. Example visualization of the color-matching algorithm for identifying an inclination angle. The circle indicates the result and the filled-in color represents the median color of the grain at maximum brightness. The cross indicates the inclination angle identified using the Rigsby stage technique. Note that ice thickness was 0.80 mm with a tolerance of 0.05 mm for relaxation in the color-matching algorithm.

larger impacts of impurities is the effect on the apparent thickness of the specimen in the vicinity of the impurity, namely that an air pocket means less ice thickness or variation in the thickness of a given ice grain. This discontinuity within a grain or between grain boundaries may be identified and isolated from the general analysis.

The thickness of the thin section has a major impact on the interference colors observed in the ice. Variations in the thickness on the order of 0.1 mm can be easily distinguished and can lead to errors in color matching. To avoid this error, the thickness of the thin section should ideally be measured over the whole specimen. Practically, several measurements can be made of the thickness around the edges of the specimen and the thickness field can be interpolated from the edge measurements and then used to calibrate the color look-up table when estimating the inclination angles of the grains. In this study, variations in thin section thickness are caused by 1) the levelness and thickness spatial fluctuations of the acrylic plate onto which the ice is welded; and 2) spatial fluctuations in the CNC machine axes. Another issue is the machining effects from the milling process. If the milling bit is not perfectly level, then an uneven milling pass will occur, causing a thickness difference between passes of the milling bit and visual stripes in the ice, depending on factors like rotational and translational speed. Moreover, milling grooves are also visible and can cause a cloudiness of the ice surface. These errors can be reduced slightly by melting the surface of the ice with a hair dryer, but this process is difficult to control and extreme care must be taken because over-melting can result in an even rougher surface. Polishing of the thin section surface by bare hand can also be performed, but proves challenging with large thin sections of 200 by 200 mm, especially when the ice temperature is below -10°C . Uneven wiping, fingerprints, or other blemishes can be easily caused when using the hand or fingers to smoothen the ice surface.

5.3. Recommendations

Improvement to *ColorIce* entails the addition of photographs taken with a wave plate added between the thin section and the analyzer (e.g. Heilbronner and Barrett (2014); Peternell et al. (2011); Wilen et al. (2003)). The wave plate reduces the four-fold symmetry of the interference coloration to two-fold symmetry based on additive and

subtractive birefringence. Furthermore, if each grain possesses a dominant geometrical orientation, or clear orientation of platelet substructure as in the case of saline ice (e.g. Weeks and Hamilton (1962)), then the *c*-axis of the grain can be compared with the geometrical orientation to resolve the four-fold symmetry to two-fold symmetry. This analysis can be performed with *ColorIce* and is planned for further development. Finally, the color-matching algorithm requires adaptation to avoid misidentification of inclination angles. The mean error for the inclination angles can be markedly reduced with such an improvement.

6. Conclusion

The theory of interference coloration was developed for visualization purposes and for rendering simulated ice types for identification purposes. The *ColorIce* tool based on interference coloration of thin sections was compared with the Rigsby stage technique, and example results were demonstrated for freshwater lake and laboratory-grown ice. The method is compatible with universal stages and polariscopes using any digital camera setup, and yields complete ice texture and quarter fabric diagrams for quantitative analysis. Albeit the ice fabrics are not complete, the quarter fabrics grant comparative information about relative grain orientations when universal stages and other specialized equipment are not available. With a mean standard deviation of inclination angle from the Rigsby stage technique of 5.4° , the mean (standard deviation of) inclination and azimuth errors of 11.5° (8.0°) and 2.9° (1.0°), respectively, demonstrate sufficient accuracy for *ColorIce*. Recommendations to improve the method include additional photographs with a wave plate, and developing the color-matching algorithm to avoid misidentification of similar interference colors.

CRediT authorship contribution statement

Cody C. Owen: Conceptualization, Methodology, Software, Validation, Formal analysis, Investigation, Resources, Data curation, Writing – original draft, Visualization. **Hayo Hendrikse:** Resources, Writing – review & editing, Funding acquisition.

Funding

This work was supported by TKI-Energy by the ‘Toeslag voor Topconsortia voor Kennis en Innovatie (TKI’s)’ of the Dutch Ministry of Economic Affairs and Climate Policy. (grant reference: TKITOE_WOZ_1906_TUD_SHIVER).

Declaration of Competing Interest

The authors declare that they have no known competing financial interests or personal relationships that could have appeared to influence the work reported in this paper.

Data availability

The data and code are available here: <https://doi.org/10.4121/19824067.v1>.

Acknowledgements

The authors thank the participating organizations in the SHIVER project: TU Delft, Siemens Gamesa Renewable Energy, and Aalto University, for supporting this work. The SHIVER project is co-financed by Siemens Gamesa Renewable Energy and TKI-Energy by the ‘Toeslag voor Topconsortia voor Kennis en Innovatie (TKI’s)’ of the Dutch Ministry of Economic Affairs and Climate Policy. The authors also thank Jeroen Koning for the detailed design and construction of the polariscope. The authors are grateful to Anne Lammertsma for assisting with the preparation of the IJsselmeer ice thin sections, and to Tim C.

Hammer and Tom Willems for drilling the IJsselmeer ice cores. The authors would also like to thank Knut Høyland and Vegard Hornnes for

the invitation to NTNU to conduct experiments with their Rigsby stage and for growing the ice.

Appendix A. Refractive indices for ice

See Table A.1 for a list of refractive indices for ice compiled from several sources.

Table A.1
Refractive indices of freshwater ice as a function of visible light wavelength for the ordinary and extraordinary rays (Heilbronner and Barrett, 2014; Hobbs, 1974; Petrenko and Whitworth, 1999).

	Visible light wavelength [nm]	Ordinary ray refractive index n_o [–]	Extraordinary ray refractive index n_e [–]
Ice at unknown temperature (Heilbronner and Barrett, 2014)	486.134	1.31335	1.31473
	527.039	1.31140	1.31276
	535.100	1.31098	1.31242
	589.594	1.30911	1.31041
	656.281	1.30715	1.30861
	670.800	1.30669	1.30802
	686.719	1.30645	1.30775
	759.370	1.30496	1.30626
	405	1.3185	1.3200
	436	1.3161	1.3176
Ice at –3.6°C (Petrenko and Whitworth, 1999)	492	1.3128	1.3143
	546	1.3105	1.3119
	589	1.3091	1.3105
	624	1.3082	1.3096
	691	1.3067	1.3081
	404.596	1.3183	1.3198
	435.806	1.3159	1.3174
	486.098	1.3129	1.3143
	491.594	1.3126	1.314
	546.090	1.3104	1.3118
Ice at –3°C (Hobbs, 1974)	578.001	1.3093	1.3107
	589.310	1.3090	1.3104
	623.403	1.3079	1.3093
	656.297	1.3070	1.3084
	690.799	1.3063	1.3077
	706.514	1.3060	1.3074

References

Adobe Systems, 2005. Adobe RGB (1998) Color Image Encoding, 2704. Adobe Syst. Inc., pp. 1–20

Azuma, N., 1994. A flow law for anisotropic ice and its application to ice sheets. *Earth Planet. Sci. Lett.* 128, 601–614. [https://doi.org/10.1016/0012-821X\(94\)90173-2](https://doi.org/10.1016/0012-821X(94)90173-2).

Azuma, N., 1995. A flow law for anisotropic polycrystalline ice under uniaxial compressive deformation. *Cold Reg. Sci. Technol.* 23, 137–147. [https://doi.org/10.1016/0165-232X\(94\)00011-L](https://doi.org/10.1016/0165-232X(94)00011-L).

Barrette, P., Michel, B., Stander, E., 1993. On the reproduction of ice from a common seed. *J. Cryst. Growth* 131, 153–156. [https://doi.org/10.1016/0022-0248\(93\)90408-O](https://doi.org/10.1016/0022-0248(93)90408-O).

Bloss, F.D., 1961. *An Introduction to the Methods of Optical Crystallography*. Saunders College Publishing.

Chauve, T., Montagnat, M., Vacher, P., 2015. Strain field evolution during dynamic recrystallization nucleation; a case study on ice. *Acta Mater.* 101, 116–124. <https://doi.org/10.1016/j.actamat.2015.08.033>.

Chauve, T., Montagnat, M., Lachaud, C., Georges, D., Vacher, P., 2017. Strain field evolution at the ductile-to-brittle transition: a case study on ice. *Solid Earth* 8, 943–953. <https://doi.org/10.5194/se-8-943-2017>.

Cole, D.M., 1998. Modeling the cyclic loading response of sea ice. *Int. J. Solids Struct.* 35, 4067–4075. [https://doi.org/10.1016/S0020-7683\(97\)00301-6](https://doi.org/10.1016/S0020-7683(97)00301-6).

Cole, D.M., Johnson, R.A., Durell, G.D., 1998. Cyclic loading and creep response of aligned first-year sea ice. *J. Geophys. Res. Ocean* 103, 21751–21758. <https://doi.org/10.1029/98JC01265>.

Durand, G., Gagliardini, O., Thorsteinsson, T., Svensson, A., Kipfstuhl, S., Dahl-Jensen, D., 2006. Ice microstructure and fabric: an up-to-date approach for measuring textures. *J. Glaciol.* 52, 619–630. <https://doi.org/10.3189/172756506781828377>.

Eicken, H., 1993. Automated image analysis of ice thin sections — instrumentation, methods and extraction of stereological and textural parameters. *J. Glaciol.* 39, 341–352. <https://doi.org/10.3189/S0022143000016002>.

Forsberg, C.H., 2021. Radiation heat transfer. In: *Heat Transfer Principles and Applications*. Elsevier, pp. 343–389. <https://doi.org/10.1016/B978-0-12-802296-2.00009-3>.

Fuerten, F., Goodchild, J.S., 2001. Quartz c-axes orientation determination using the rotating polarizer microscope. *J. Struct. Geol.* 23, 895–902. [https://doi.org/10.1016/S0191-8141\(00\)00161-9](https://doi.org/10.1016/S0191-8141(00)00161-9).

Gay, M., Weiss, J., 1999. Automatic reconstruction of polycrystalline ice microstructure from image analysis: application to the EPICA ice core at Dome Concordia, Antarctica. *J. Glaciol.* 45, 547–554. <https://doi.org/10.1017/S0022143000001416>.

Georges, D., Saletti, D., Montagnat, M., Forquin, P., Hagenmuller, P., 2021. Influence of porosity on ice dynamic tensile behavior as assessed by spalling tests. *J. Dyn. Behav. Mater.* 7, 575–590. <https://doi.org/10.1007/s40870-021-00300-z>.

Ghararni, I.E., Dempsey, J.P., Polojärvi, A., Tuhturi, J., 2021. Fracture of warm S2 columnar freshwater ice: size and rate effects. *Acta Mater.* 202, 22–34. <https://doi.org/10.1016/j.actamat.2020.10.031>.

Gonzalez, R.C., Woods, R.E., 2008. *Digital Image Processing Third Edition*, 3rd ed (Digital Image Processing).

Goodchild, J.S., Fuerten, F., 1998. Edge detection in petrographic images using the rotating polarizer stage. *Comput. Geosci.* 24, 745–751. [https://doi.org/10.1016/S0098-3004\(98\)00054-5](https://doi.org/10.1016/S0098-3004(98)00054-5).

Grennerat, F., Montagnat, M., Castelnau, O., Vacher, P., Moulinec, H., Suquet, P., Duval, P., 2012. Experimental characterization of the intragranular strain field in columnar ice during transient creep. *Acta Mater.* 60, 3655–3666. <https://doi.org/10.1016/j.actamat.2012.03.025>.

Hansen, D.P., Wilen, L.A., 2002. Performance and applications of an automated c -axis ice-fabric analyzer. *J. Glaciol.* 48, 159–170. <https://doi.org/10.3189/172756502781831566>.

Heilbronner, R., Barrett, S., 2014. *Image Analysis in Earth Sciences, Geotectonic Research*. Springer Berlin Heidelberg, Berlin, Heidelberg. <https://doi.org/10.1007/978-3-642-10343-8>.

Heilbronner, R.P., Pauli, C., 1993. Integrated spatial and orientation analysis of quartz c-axes by computer-aided microscopy. *J. Struct. Geol.* 15, 369–382. [https://doi.org/10.1016/0191-8141\(93\)90133-U](https://doi.org/10.1016/0191-8141(93)90133-U).

Hendrikse, H., Hammer, T.C., van den Berg, M., Willems, T., Owen, C.C., van Beek, K., Ebben, N.J.J., Puolakka, O., Polojärvi, A., 2022. Experimental data from ice basin tests with vertically sided cylindrical structures. *Data Br.* 41 <https://doi.org/10.1016/j.dib.2022.107877>, 107877.

Hill, J.R., Lasca, N.P., 1971. An improved method for determining ice fabrics. *J. Glaciol.* 10, 133–138. <https://doi.org/10.1017/S0022143000013071>.

- Hobbs, P.V., 1974. *Ice Physics*. Clarendon Press, Oxford.
- Iliescu, D., Baker, I., Chang, H., 2004. Determining the orientations of ice crystals using electron backscatter patterns. *Microsc. Res. Tech.* 63, 183–187. <https://doi.org/10.1002/jemt.20029>.
- Kamb, W.B., 1962. Refraction corrections for universal stage measurements. I. Uniaxial crystals. *Am. Mineral.* 47, 227–245.
- Lange, M.A., 1988. A computer-controlled system for ice-fabric analysis on a Rigsby stage. *Ann. Glaciol.* 10, 92–94. <https://doi.org/10.3189/S0260305500004237>.
- Langway, C.C.J., 1958. *Ice Fabrics and the Universal Stage*. U.S. Army Snow Ice and Permafrost Research Establishment, Wilmette, Illinois, USA.
- Linge Johnsen, S.A., Bollman, J., Lee, H.W., Zhou, Y., 2018. Accurate representation of interference colours (Michel-Lévy chart): from rendering to image colour correction. *J. Microsc.* 269, 321–337. <https://doi.org/10.1111/jmi.12641>.
- Melgosa, M., 2000. Testing CIELAB-based color-difference formulas. *Color. Res. Appl.* 25, 49–55. [https://doi.org/10.1002/\(SICI\)1520-6378\(200002\)25:1<49::AID-COL7>3.0.CO;2-4](https://doi.org/10.1002/(SICI)1520-6378(200002)25:1<49::AID-COL7>3.0.CO;2-4).
- Michel, B., Ramseier, R.O., 1971. Classification of river and lake ice. *Can. Geotech. J.* 8, 36–45. <https://doi.org/10.1139/t71-004>.
- Montagnat, M., Bourcier, M., Philip, A., Bons, P.D., Bauer, C.C., Deconinck, P., Hereil, P., 2021. Texture characterization of some large hailstones with an automated technique. *J. Glaciol.* 67, 1190–1204. <https://doi.org/10.1017/jog.2021.66>.
- Monz, M.E., Hudleston, P.J., Prior, D.J., Michels, Z., Fan, S., Negrini, M., Langhorne, P.J., Qi, C., 2021. Full crystallographic orientation (c and a axes) of warm, coarse-grained ice in a shear-dominated setting: a case study, Storglaciären, Sweden. *Cryosphere* 15, 303–324. <https://doi.org/10.5194/tc-15-303-2021>.
- Morgan, V.I., Davis, E.R., Wehrle, E., 1984. A Rigsby stage with remote computer compatible output. *Cold Reg. Sci. Technol.* 10, 89–92. [https://doi.org/10.1016/0165-232X\(84\)90036-3](https://doi.org/10.1016/0165-232X(84)90036-3).
- Murphy, D.B., 2001. *Fundamentals of Light Microscopy and Electronic Imaging*, First edit. ed. John Wiley & Sons, Inc.
- O'Connor, D., West, B., Haehnel, R., Asenath-Smith, E., Cole, D., 2020. A viscoelastic integral formulation and numerical implementation of an isotropic constitutive model of saline ice. *Cold Reg. Sci. Technol.* 171, 102983. <https://doi.org/10.1016/j.coldregions.2019.102983>.
- O'Rourke, B.J., Jordaan, I.J., Taylor, R.S., Gürtner, A., 2016. Experimental investigation of oscillation of loads in ice high-pressure zones, part 1: single indenter system. *Cold Reg. Sci. Technol.* 124, 25–39. <https://doi.org/10.1016/j.coldregions.2015.12.005>.
- Pascale, D., 2003. A Review of RGB Color Spaces... from xyY to R'G'B'. *The BabelColor Company*, Montréal, Quebec, Canada.
- Pauling, L., 1935. The structure and entropy of ice and of other crystals with some randomness of atomic arrangement. *J. Am. Chem. Soc.* 57, 2680–2684. <https://doi.org/10.1021/ja01315a102>.
- Perey, F.G.J., Pounder, E.R., 1958. Crystal orientation in ice sheets. *Can. J. Phys.* 36, 494–502. <https://doi.org/10.1139/p58-050>.
- Peternell, M., Russell-Head, D.S., Wilson, C.J.L., 2011. A technique for recording polycrystalline structure and orientation during in situ deformation cycles of rock analogues using an automated fabric analyser. *J. Microsc.* 242, 181–188. <https://doi.org/10.1111/j.1365-2818.2010.03456.x>.
- Peternell, M., Dierckx, M., Wilson, C.J.L., Piazzolo, S., 2014. Quantification of the microstructural evolution of polycrystalline fabrics using FAME: application to in situ deformation of ice. *J. Struct. Geol.* 61, 109–122. <https://doi.org/10.1016/j.jsg.2013.05.005>.
- Petrenko, V.F., Whitworth, R.W., 1999. *Physics of Ice*. Oxford University Press, New York. <https://doi.org/10.1093/acprof:oso/978019518945.001.0001>.
- Pounder, E.R., 1965. *Physics of Ice*. Pergamon Press, Oxford.
- Price, G.P., 1973. The photometric method in microstructural analysis. *Am. J. Sci.* 273, 523–537. <https://doi.org/10.2475/ajs.273.6.523>.
- Raith, M.M., Raase, P., Reinhardt, J., 2012. *Guide to Thin Section Microscopy*, Second. ed. Mineral Society of America.
- Rigsby, G.P., 1951. *Crystal fabric studies on Emmons Glacier Mount Rainier*, Washington. *J. Geol.* 59, 590–598.
- Sammonds, P., Montagnat, M., Bons, P., Schneebeli, M., 2017. Ice microstructures and microdynamics. *Philos. Trans. R. Soc. A Math. Phys. Eng. Sci.* 375, 5. <https://doi.org/10.1098/rsta.2016.0438>.
- Schulson, E.M., Duval, P., 2009. *Creep and Fracture of Ice*. Cambridge University Press. <https://doi.org/10.1017/CBO9780511581397>.
- Schwarz, J., Weeks, W.F., 1977. Engineering properties of sea ice. *J. Glaciol.* 19, 499–531. <https://doi.org/10.3189/S0022143000029476>.
- Seidemann, M., Prior, D.J., Golding, N., Durham, W.B., Lilly, K., Vaughan, M.J., 2020. The role of kink boundaries in the deformation and recrystallisation of polycrystalline ice. *J. Struct. Geol.* 136, 104010. <https://doi.org/10.1016/j.jsg.2020.104010>.
- Seymour-Pierce, A., Lishman, B., Sammonds, P., 2017. Recrystallization and damage of ice in winter sports. *Philos. Trans. R. Soc. A Math. Phys. Eng. Sci.* 375, 20150353. <https://doi.org/10.1098/rsta.2015.0353>.
- Shestov, A., 2018. Birefringence in ice crystals. Principles and application in sea ice microstructure studies. In: *Arbatskaia, G. (Ed.), Proceedings of the 24th IAHR International Symposium on Ice*. IAHR, Vladivostok, Russia, pp. 248–257.
- Shokr, M., Sinha, N.K., 2015. *Sea ice: Physics and Remote Sensing*. Jogn Wiley & Sons Inc., Hoboken, New Jersey, USA.
- Sinha, N.K., 1977. Technique for studying structure of sea ice. *J. Glaciol.* 18, 315–324. <https://doi.org/10.3189/S0022143000021390>.
- Sinha, N.K., 2011. Borehole indenter - a tool for assessing in-situ bulk ice strength and micromechanics. *Cold Reg. Sci. Technol.* 69, 21–38. <https://doi.org/10.1016/j.coldregions.2011.07.009>.
- Snyder, S.A., Schulson, E.M., Renshaw, C.E., 2015. The role of damage and recrystallization in the elastic properties of columnar ice. *J. Glaciol.* 61, 461–480. <https://doi.org/10.3189/2015JoG14J225>.
- Sopper, R., Daley, C., Colbourne, B., Bruneau, S., 2017. The influence of water, snow and granular ice on ice failure processes, ice load magnitude and process pressure. *Cold Reg. Sci. Technol.* 139, 51–64. <https://doi.org/10.1016/j.coldregions.2017.04.006>.
- Sørensen, B.E., 2013. A revised Michel-Lévy interference colour chart based on first-principles calculations. *Eur. J. Mineral.* 25, 5–10. <https://doi.org/10.1127/0935-1221/2013/0025-2252>.
- Stockman, A., Rider, A., Henning, B., Baabab, R., Mylonas, D., Andrikopoulos, P., 2020. CVRL Database [WWW Document]. Colour Vis. Res. Lab. URL: <http://cvrl.ioo.ucl.ac.uk/index.htm>. accessed 3.25.20.
- Thorsteinsson, T., Kipfstuhl, J., Miller, H., 1997. Textures and fabrics in the GRIP ice core. *J. Geophys. Res. Ocean.* 102, 26583–26599. <https://doi.org/10.1029/97JC00161>.
- Timco, G.W., Weeks, W.F., 2010. A review of the engineering properties of sea ice. *Cold Reg. Sci. Technol.* 60, 107–129. <https://doi.org/10.1016/j.coldregions.2009.10.003>.
- Weeks, W.F., Hamilton, W.L., 1962. Petrographic characteristics of young sea ice, point barrow, Alaska. *Am. Mineral.* 47, 945–961.
- Weeks, W.F., Hibler III, W.D., 2010. *On Sea Ice*. University of Alaska Press, Fairbanks.
- Wei, M., Polojärvi, A., Cole, D.M., Prasanna, M., 2020. Strain response and energy dissipation of floating saline ice under cyclic compressive stress. *Cryosphere* 14, 2849–2867. <https://doi.org/10.5194/tc-14-2849-2020>.
- Wei, M., Prasanna, M., Cole, D.M., Polojärvi, A., 2022. Response of dry and floating saline ice to cyclic compression. *Geophys. Res. Lett.* 49, 1–10. <https://doi.org/10.1029/2022GL099457>.
- Wilen, L.A., 2000. A new technique for ice-fabric analysis. *J. Glaciol.* 46, 129–139. <https://doi.org/10.3189/172756500781833205>.
- Wilen, L.A., Diprinzio, C.L., Alley, R.B., Azuma, N., 2003. Development, principles, and applications of automated ice fabric analyzers. *Microsc. Res. Tech.* 62, 2–18. <https://doi.org/10.1002/jemt.10380>.
- Wilson, C.J.L., Peternell, M., 2011. Evaluating ice fabrics using fabric analyser techniques in Sørsdal Glacier, East Antarctica. *J. Glaciol.* 57, 881–894. <https://doi.org/10.3189/002214311798043744>.
- Yadegari, S., Turteltaub, S., Suiker, A.S.J., Kok, P.J.J., 2014. Analysis of banded microstructures in multiphase steels assisted by transformation-induced plasticity. *Comput. Mater. Sci.* 84, 339–349. <https://doi.org/10.1016/j.commatsci.2013.12.002>.
- Yun, W., Azuma, N., 1999. A new automatic ice-fabric analyzer which uses image-analysis techniques. *Ann. Glaciol.* 29, 155–162. <https://doi.org/10.3189/172756499781821021>.